Article

Cell Reports

Cell-Type Specificity of Callosally Evoked Excitation and Feedforward Inhibition in the Prefrontal Cortex

Graphical Abstract

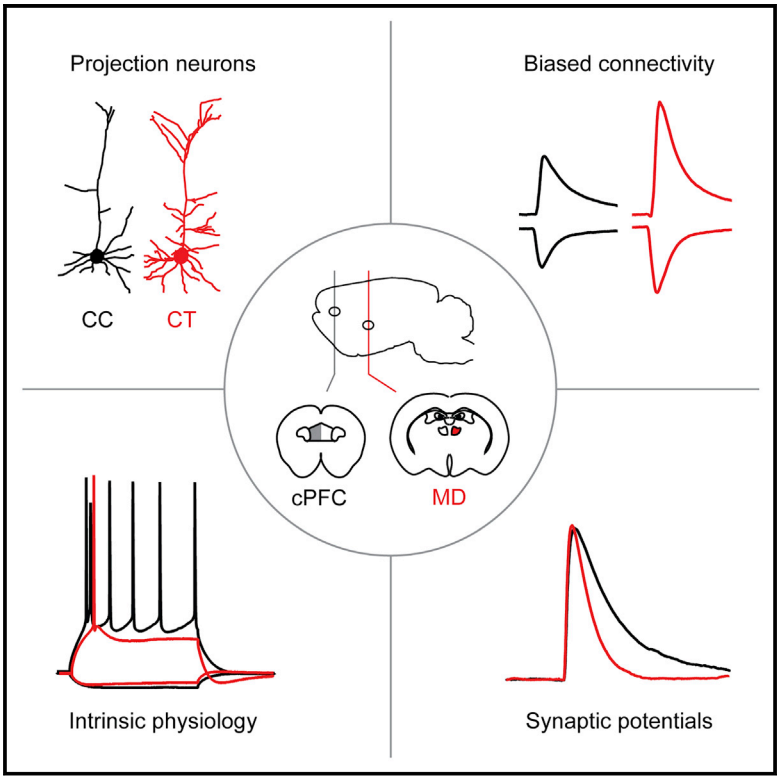

Authors

Paul G. Anastasiades, Joseph J. Marlin, Adam G. Carter

Correspondence

adam.carter@nyu.edu

In Brief

Anastasiades et al. explore the functional significance of differences in synaptic connectivity and intrinsic physiology at two classes of layer 5 projection neurons in the prefrontal cortex (PFC). They find subthreshold and suprathreshold responses depend on cell-type-specific connectivity and physiology, which combine to influence synaptic responses and evoked firing.

Highlights

- L5 projection neurons have distinct morphology and intrinsic physiology in the PFC
- Callosal excitation and feedforward inhibition is much stronger at CT neurons
- Intrinsic properties equalize synaptic inputs and accelerate decays at CT neurons
- Biased connectivity is needed to maintain balanced firing at CC and CT neurons

Anastasiades et al., 2018, Cell Reports *22*, 679–692
January 16, 2018
https://doi.org/10.1016/j.celrep.2017.12.073

CellPress

Cell Reports
Article

Cell-Type Specificity of Callosally Evoked Excitation and Feedforward Inhibition in the Prefrontal Cortex

Paul G. Anastasiades,[1] Joseph J. Marlin,[1] and Adam G. Carter[1,2,*]
[1]Center for Neural Science, New York University, 4 Washington Place, New York, NY 10003, USA
[2]Lead Contact
*Correspondence: adam.carter@nyu.edu
https://doi.org/10.1016/j.celrep.2017.12.073

SUMMARY

Excitation and inhibition are highly specific in the cortex, with distinct synaptic connections made onto subtypes of projection neurons. The functional consequences of this selective connectivity depend on both synaptic strength and the intrinsic properties of targeted neurons but remain poorly understood. Here, we examine responses to callosal inputs at cortico-cortical (CC) and cortico-thalamic (CT) neurons in layer 5 of mouse prelimbic prefrontal cortex (PFC). We find callosally evoked excitation and feedforward inhibition are much stronger at CT neurons compared to neighboring CC neurons. Elevated inhibition at CT neurons reflects biased synaptic inputs from parvalbumin and somatostatin positive interneurons. The intrinsic properties of postsynaptic targets equalize excitatory and inhibitory response amplitudes but selectively accelerate decays at CT neurons. Feedforward inhibition further reduces response amplitude and balances action potential firing across these projection neurons. Our findings highlight the synaptic and cellular mechanisms regulating callosal recruitment of layer 5 microcircuits in PFC.

INTRODUCTION

Cortical pyramidal neurons communicate with other brain regions via diverse long-range projections (Gabbott et al., 2005; Harris and Shepherd, 2015). Different classes of pyramidal neurons possess unique morphology, intrinsic physiology, and synaptic properties (Brown and Hestrin, 2009; Hattox and Nelson, 2007; Larkman and Mason, 1990; Le Bé et al., 2007; Mason and Larkman, 1990; Morishima and Kawaguchi, 2006). For example, in layer 5 of the mouse prefrontal cortex (PFC), cortico-cortical (CC) neurons that project to the contralateral hemisphere are intermingled with cortico-thalamic (CT) neurons that project to the thalamus (Gee et al., 2012). Determining how these subnetworks of neurons are activated is necessary for understanding cortical function.

Pyramidal neurons process long-range excitatory inputs from a variety of cortical and subcortical structures (Hooks et al., 2013; Petreanu et al., 2009). Recent studies indicate that these inputs often make unique connections onto different populations of projection neurons (Little and Carter, 2013; Mao et al., 2011; Suter and Shepherd, 2015; Yamawaki and Shepherd, 2015). Callosal inputs from the contralateral hemisphere are prominent throughout the cerebral cortex, indicating an essential role (Carr and Sesack, 1998; Czeiger and White, 1993; Fame et al., 2011; Ferino et al., 1987). These inputs enable direct communication between hemispheres and are responsible for coordinating behavior (Hasegawa et al., 1998; Li et al., 2016). However, the targeting and functional influence of callosal inputs at different projection neurons remains unresolved in the PFC.

Excitatory inputs to the cortex evoke pronounced inhibitory responses via local GABAergic interneurons (Cruikshank et al., 2007, 2010; Isaacson and Scanziani, 2011; Karayannis et al., 2007; Rock and Apicella, 2015). Feedforward inhibition is often mediated by parvalbumin-expressing (PV^+) interneurons (Cruikshank et al., 2007; Delevich et al., 2015; Rock and Apicella, 2015) and can strongly regulate both subthreshold responses and suprathreshold activity (Isaacson and Scanziani, 2011; Pouille et al., 2009). Neurons that project to subcortical regions receive stronger PV^+ inputs, and therefore greater feedforward inhibition (Lee et al., 2014a; Ye et al., 2015). However, it is uncertain whether other inhibitory inputs exhibit similar targeting, including somatostatin-expressing (SOM^+) interneurons that typically mediate feed-back inhibition (Kapfer et al., 2007; Silberberg and Markram, 2007). More generally, the functional impact of this biased inhibition at different populations of pyramidal neurons remains unclear.

In addition to receiving distinct inputs, pyramidal neurons display a wide variety of intrinsic properties that often depend on their projection targets (Hattox and Nelson, 2007; Le Bé et al., 2007; Mason and Larkman, 1990). CT neurons in layer 5 possess a robust hyperpolarization-activated cation current (h-current), which can strongly regulate the amplitude and decay of synaptic responses (Berger et al., 2001; Magee, 2000; Williams and Stuart, 2000, 2003). CC neurons largely lack h-current and consequently have much higher input resistance (Dembrow et al., 2010), which may enhance the amplitude of synaptic responses (George et al., 2009; Sheets et al., 2011) and influence their kinetics. However, it is unclear how intrinsic properties sculpt subthreshold excitation and inhibition at

different subtypes of pyramidal neurons. Moreover, the relative impact of differences in intrinsic physiology and feedforward inhibition on evoked firing has not been established.

Here, we examine how callosal inputs evoke excitation and feedforward inhibition at CC and CT neurons in layer 5 of the mouse PFC. We find callosal inputs evoke larger excitatory and inhibitory conductances at CT neurons compared to CC neurons. Differences in feedforward inhibition are explained by biased connections onto CT neurons from both PV^+ and SOM^+ interneurons. Intrinsic properties equalize both excitatory and inhibitory potentials but selectively accelerate their decays at CT neurons. Feedforward inhibition can also accelerate decays but primarily reduces response amplitude and suppresses firing. Together, our findings define the specificity of excitatory and inhibitory connectivity at distinct classes of pyramidal neurons, revealing important wiring rules in the PFC. More broadly, they demonstrate how intrinsic and synaptic properties combine to determine the postsynaptic responses to callosal inputs, and how their synergistic functions maintain balanced output across multiple projection pathways.

RESULTS

Callosal Inputs Evoke Biased Excitation and Feedforward Inhibition

We examined synaptic responses to callosal inputs at neighboring layer 5 (L5) CC and CT neurons in the prelimbic (PL) region of the mouse PFC. In order to target these inputs, we injected AAVs expressing fluorescently tagged ChR2 into the contralateral PFC (cPFC) (Figure 1A) and observed pronounced anterograde labeling across multiple layers, including L5 (Figure 1B). To identify the two cell types, we simultaneously co-injected fluorescent tracers (CTBs) into the cPFC and ipsilateral mediodorsal thalamus (MD) (Figure 1A). While CC neurons were located more superficially, and CT neurons were restricted to deep layers, both cell types resided in L5, where they constituted intermingled yet distinct populations (Figures 1B and S1B; co-labeling = 1/340 cells, 0.8% of CC, 0.5% of CT). Interestingly, a subset of L5 CT neurons overlapped with cortico-pontine (CP) neurons (23.3% of PT, 36.6% of CT), suggesting that CT neurons can also signal via the pyramidal tract (Figures S1A and S1B) (Deschênes et al., 1994; Lévesque et al., 1996).

We next assessed whether callosal inputs exhibit any preferential targeting of L5 CC or CT neurons in the PFC. Using whole-cell recordings, we found that CT neurons have more extensive dendrites than CC neurons, suggesting that they could differentially sample inputs from the contralateral hemisphere (Figures 1C, S1C, and S1D). We next used optogenetics to compare cPFC-evoked synaptic responses at neighboring cells, which helps account for any variability in ChR2 expression between slices and animals (Anastasiades et al., 2017; Little and Carter, 2013). Initially, we isolated monosynaptic connections by recording in TTX (1 μM) and 4-AP (100 μM), which prevents polysynaptic activation of the local network but preserves pathway-specific glutamate release (Little and Carter, 2013; Petreanu et al., 2009). We found that callosal inputs evoked robust excitatory postsynaptic currents (EPSCs) (Figure 1D), which were much stronger at CT neurons (Figure 1E; EPSC: CC = 91 ± 27 pA, CT = 140 ± 22 pA, p = 0.03). Taking the ratio of EPSC amplitudes accounted for variability across experiments and revealed inputs were twice as strong at CT neurons (Figure 1E; CT/CC amplitude ratio = 2.0, CI: 1.1–3.4, p = 0.03), indicating that callosal inputs preferentially target these cells.

Recent studies at other populations of layer 5 pyramidal neurons suggest that dendritic targeting may contribute to the strength of callosally evoked EPSCs (Rock and Apicella, 2015). To assess subcellular targeting, we mapped the strength of callosal inputs across the dendrites of CC and CT neurons (Mao et al., 2011; Petreanu et al., 2009) (Figure S1E). Callosal inputs evoked strong EPSCs at the soma, which decreased in amplitude and slowed in kinetics in the dendrites (Figures S1E and S1F). However, CC and CT neurons showed similar distributions of normalized EPSC amplitude at different dendritic locations (Figures S1E and S1F), suggesting that differences in subcellular targeting do not mediate the bias in cPFC input.

In addition to direct excitation, inputs to cortex can evoke feedforward inhibition, which could also strongly influence postsynaptic responses at both CC and CT neurons (Cruikshank et al., 2007, 2010; Isaacson and Scanziani, 2011). Using optogenetic stimulation in the absence of TTX and 4-AP, we recorded EPSCs at −70 mV and inhibitory postsynaptic currents (IPSCs) at +10 mV. Both EPSCs and IPSCs were robustly evoked at CC and CT neurons, and their magnitude increased with light pulse duration (Figure 1F). Moreover, IPSCs followed EPSCs at short latency, consistent with feedforward, rather than direct, inhibition (EPSC-IPSC latency: CC = +3.4 ± 0.6 ms, CT = +4.4 ± 0.5 ms). Interestingly, inhibition mirrored excitation, with both EPSCs and IPSCs much stronger onto CT neurons compared to neighboring CC neurons (Figure 1G; EPSC: CC = 134 ± 33 pA, CT = 247 ± 37 pA, p = 0.005; IPSC: CC = 210 ± 73 pA, CT = 421 ± 80 pA, p = 0.01). These findings indicate that callosal inputs evoke excitation and feedforward inhibition that is strongly biased onto L5 CT neurons.

Callosal Inputs Engage Both PV^+ and SOM^+ Interneurons

In other areas of cortex, callosal inputs often evoke feedforward inhibition by activating PV^+ interneurons (Karayannis et al., 2007; Rock and Apicella, 2015). However, recent studies indicate that SOM^+ interneurons can also be recruited by long-range afferents to the PFC (McGarry and Carter, 2016). To selectively label PV^+ and SOM^+ interneurons, we injected Cre-dependent viruses into the PFC of PV-Cre or SOM-Cre mice. Both PV^+ and SOM^+ interneurons were observed in L5 of the PFC (Figure 2A) and displayed characteristic firing properties (Figures S2A and S2B). To assess whether the cPFC made connections onto PV^+ or SOM^+ interneurons, we initially used a conditional rabies virus strategy (Wickersham et al., 2007) (Figure 2B). We first injected helper AAV1-CA-FLEX-RG and AAV1-EF1a-FLEX-TVA-Cherry into the PFC. After allowing for expression, we then injected SADΔG-GFP(EnvA) rabies virus to label presynaptic cells that contact these interneurons (Figures 2B and S2C). We observed GFP-labeled neurons in the cPFC of both transgenic mice (Figure 2B), indicating that these interneurons receive monosynaptic inputs.

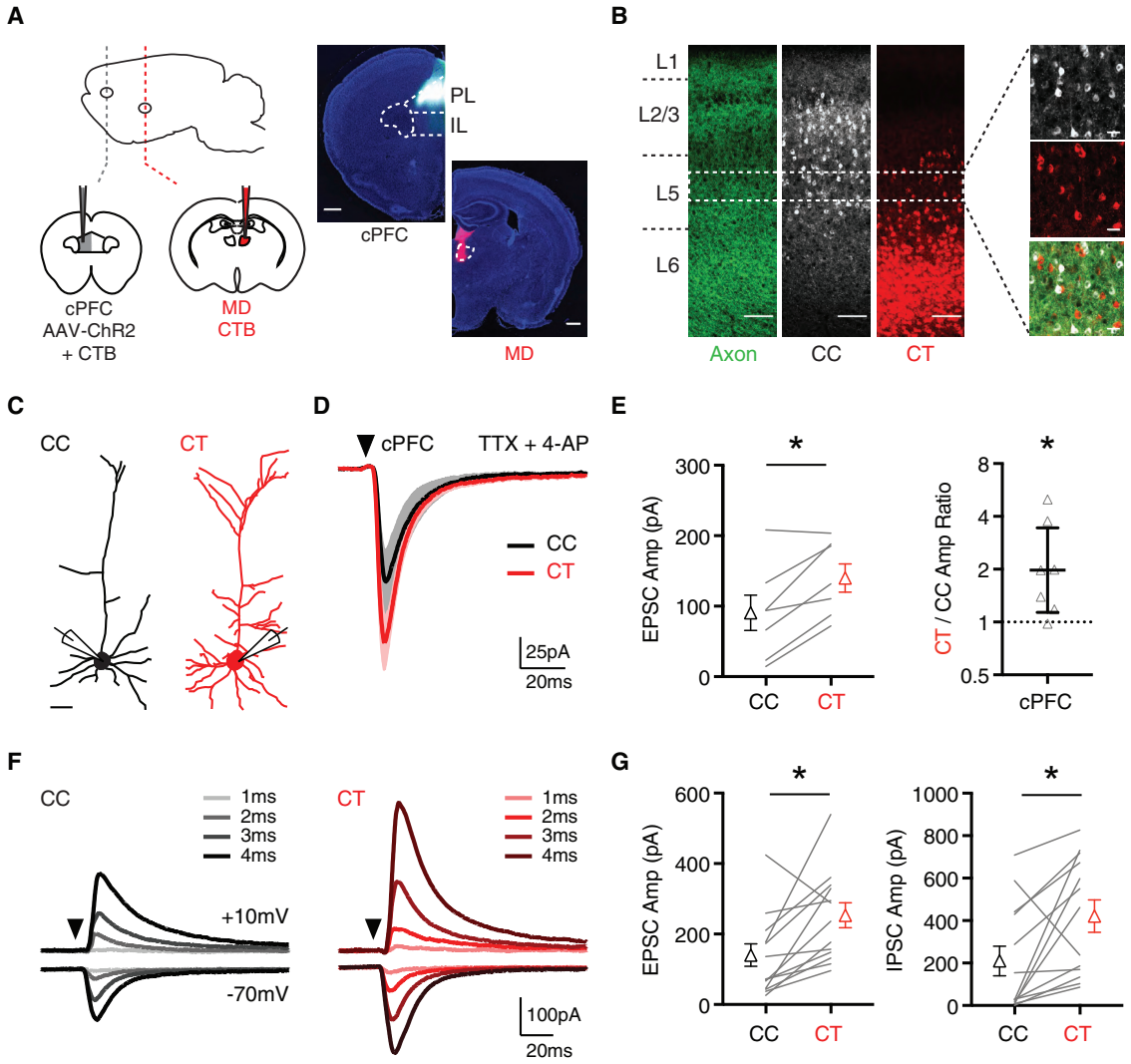

Figure 1. Callosal Inputs Evoke Stronger Excitation and Inhibition at L5 CT Neurons

(A) Left, injections of AAV-ChR2 into the contralateral PFC (cPFC) to label callosal inputs, and CTB into the cPFC or ipsilateral mediodorsal thalamus (MD) to label CC and CT neurons. Right, injection sites, with dashed regions indicating prelimbic (PL), infralimbic (IL), and MD (scale bar, 500 μm). (Representative images, n = 3 mice.)

(B) Confocal images showing the distributions of cPFC axons (left), CC neurons (middle), and CT neurons (right) across multiple layers of PL PFC (scale bar, 100 μm). Dashed white box indicates the band in layer 5 (L5) from which electrophysiological recordings were made. Far right, confocal images of CC neurons (white) CT neurons (red) and intermingled cPFC axons (green) (scale bar, 25 μm).

(C) Morphological reconstructions made from 2-photon images of CC neurons (black) and CT neurons (red) (scale bar, 50 μm).

(D) Average monosynaptic cPFC-evoked EPSCs at pairs of CC (black) and CT (red) neurons recorded in the presence of TTX and 4-AP (n = 7 pairs, 4 mice). Arrow indicates light pulse (4-ms duration).

(E) Summary of EPSC amplitudes at pairs of CC and CT neurons (left) and CT/CC amplitude ratio with y axis on log2 scale (right).

(F) Average cPFC-evoked EPSCs recorded at −70 mV and IPSCs recorded at +10 mV in CC (black) and CT (red) neurons, recorded across a range of light durations (1–4 ms) in the absence of TTX and 4-AP (n = 13 pairs, 8 mice). Traces are averages taken across all cells at each LED pulse duration.

(G) Summary of amplitudes of EPSCs (left) and IPSCs (right) recorded at pairs of CC and CT neurons in response to 4 ms light stimulation.

See also Figure S1. Values are mean ± SEM (E, left and G) or geometric mean ± CI (E, right), *p < 0.05.

We next used optogenetics to examine the functional properties of callosal inputs onto PV$^+$ and SOM$^+$ interneurons. We observed cPFC-evoked EPSCs in the presence of TTX and 4-AP, which were blocked by bath application of NBQX (10 μM) (Figures S2D and S2E), confirming that both interneurons receive monosynaptic, glutamatergic input from the cPFC. We then compared the amplitude of cPFC-evoked EPSCs at either PV$^+$ or SOM$^+$ interneurons with adjacent L5 CC neurons (Figure 2C), which allows for comparison of input strength across transgenic lines (McGarry and Carter, 2016). This revealed that PV$^+$ interneurons received stronger callosal inputs than SOM$^+$ interneurons (PV/CC amplitude ratio = 1.5, CI: 0.8–2.8, SOM/CC amplitude

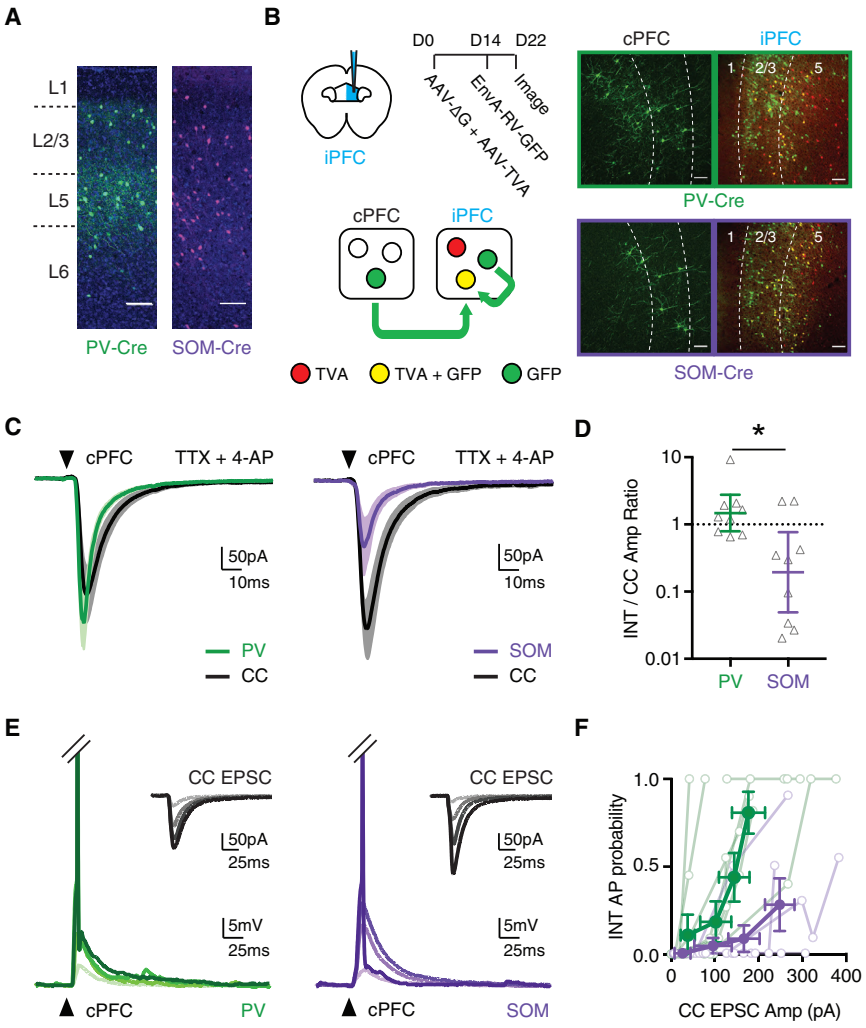

Figure 2. Both PV$^+$ and SOM$^+$ Interneurons Are Engaged by Callosal Inputs

(A) Distributions of PV$^+$ (green) and SOM$^+$ (purple) interneurons across multiple layers of prelimbic PFC, in virally injected PV-Cre and SOM-Cre mice (scale bars, 100 μm). (Representative images, n = 3 mice each for PV- and SOM-Cre.)

(B) Left, schematic of conditional rabies virus (RV) tracing, with helper AAVs injected on day 0 and RV on day 14 in the ipsilateral PFC (iPFC), followed by imaging on day 22 in the iPFC and cPFC. Right, representative anatomy for PV-Cre (top) and SOM-Cre (bottom) mice (n = 3 mice each for PV- and SOM-Cre), showing TVA$^+$ interneurons in the iPFC (red), starter interneurons in the iPFC (yellow), and connected presynaptic neurons in the iPFC and cPFC (green) (scale bar, 100 μm).

(C) Average cPFC-evoked EPSCs at pairs of CC neurons (black) and neighboring PV$^+$ interneurons (green) (n = 9 pairs, 4 mice) or SOM$^+$ interneurons (purple) (n = 9 pairs, 4 mice). Arrow indicates light pulse (4-ms duration).

(D) Summary of interneuron (INT)/CC amplitude ratio from recordings in (C), with y axis on log10 scale.

(E) cPFC-evoked EPSPs and action potentials (APs) at PV$^+$ (green) and SOM$^+$ (purple) interneurons, recorded across a range of light durations (n = 9 pairs, 5 mice for PV$^+$, n = 7 pairs, 4 mice for SOM$^+$). APs have been truncated to highlight subthreshold responses. Arrows indicate light pulse. Insets show average cPFC-evoked EPSCs at adjacent CC neurons (black). Responses shown at a range of light durations (1–4 ms), evoking cPFC input of increasing magnitude. Darker lines represent longer pulse durations.

(F) Summary of AP probability at PV$^+$ and SOM$^+$ interneurons as a function of EPSC amplitude at adjacent CC neurons. Data are shown across increasing light durations (1–4 ms), with each cell contributing 4 data points.

See also Figure S2. Values are geometric mean ± CI (D) or mean ± SEM (F), *p < 0.05.

ratio = 0.2, CI: 0.05–0.8, p = 0.03). However, a subset of SOM$^+$ interneurons received sizable responses that might also drive them to fire action potentials (APs) (Figure 2D). To test this, we performed current-clamp recordings from PV$^+$ and SOM$^+$ interneurons while recording from adjacent CC neurons in voltage clamp, to control for cPFC-evoked excitatory drive across experiments (Figure 2E). PV$^+$ interneurons (n = 8/9) were more readily driven to fire than SOM$^+$ interneurons (n = 3/7) (Figure 2F; two-way ANOVA: interaction p = 0.0015, LED duration p < 0.0001, cell type p = 0.03). Moreover, at stimulation intensities that evoked similar levels of excitation at CC neurons (Figure S2F; CC EPSC: PV = 173 ± 38 pA, SOM = 246 ± 33 pA, p = 0.14), the probability of firing APs was much higher for PV$^+$ than SOM$^+$ interneurons (Figure S2F; PV = 0.80 ± 0.12, SOM = 0.28 ± 0.15, p = 0.008). These findings indicate that both PV$^+$ and SOM$^+$ interneurons receive excitatory inputs from the cPFC, but PV$^+$ interneurons are the primary mediators of cPFC-evoked feedforward inhibition.

Biased Inhibition Reflects Cell-Type-Specific Connectivity

Previous studies in the PFC and other cortical areas indicate that PV$^+$ interneurons can make targeted connections onto unlabeled layer 5 pyramidal neurons that resemble CT neurons (Lee et al., 2014a; Ye et al., 2015), which could explain biased inhibitory targeting. However, the targeting and functional impact of SOM$^+$ interneurons remains less clear (Morishima et al., 2017). We next used conditional optogenetics to examine interneuron-specific IPSCs at adjacent CC and CT neurons. We combined retrograde labeling with injection of Cre-dependent AAV1-EF1a-DIO-hChR2(H134R)-EYFP in PV-Cre or SOM-Cre mice to target specific interneuron populations (Figure 3A). Both PV$^+$ and SOM$^+$ interneurons evoked much larger IPSCs at CT than CC neurons (Figures 3B and 3C), yielding elevated CT/CC amplitude ratios (Figure 3C; PV$^+$ = 3.8, CI: 2.3–6.3, p = 0.02; SOM$^+$ = 2.1, CI: 1.4–3.1, p < 0.001). These findings

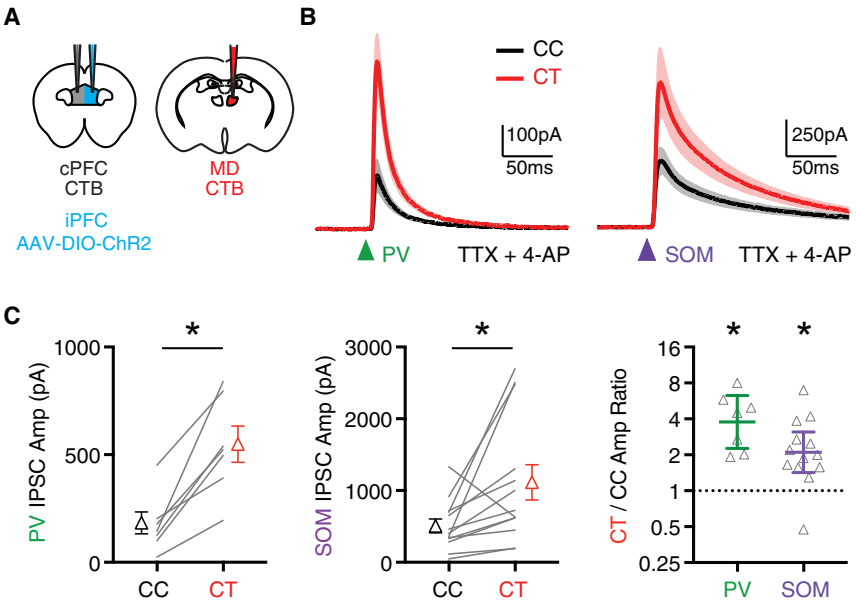

Figure 3. PV$^+$ and SOM$^+$ Interneurons Preferentially Target CT Neurons

(A) Injections used to conditionally express ChR2 in interneurons of PV-Cre or SOM-Cre mice, while also retrogradely labeling CC and CT neurons.

(B) Average IPSCs evoked by either PV$^+$ interneurons (left) or SOM$^+$ interneurons (right) at pairs of CC neurons (black) and CT (red) neurons, recorded in the presence of TTX and 4-AP (n = 7 pairs, 7 mice for PV$^+$, n = 13 pairs, 8 mice for SOM$^+$). Arrows indicate light pulse (4-ms duration).

(C) Summary of amplitudes of IPSCs evoked by PV$^+$ (left) and SOM$^+$ (middle) interneurons at pairs of CC and CT neurons. Right, summary of CT/CC amplitude ratios, with y axis on log2 scale.

See also Figure S3. Values are mean ± SEM (C, left, middle) or geometric mean ± CI (C, right), *p < 0.05.

indicate that both PV$^+$ and SOM$^+$ interneurons provide stronger input onto CT neurons, helping to explain the biased feedforward inhibition.

PV$^+$ and SOM$^+$ interneurons also target distinct subcellular domains of pyramidal neurons (Kawaguchi and Kubota, 1997; Marlin and Carter, 2014), but it is unknown whether subcellular targeting differs between cell types, and whether this contributes to synaptic strength. We next tested whether these interneurons make unique connections in the dendrites of CC and CT neurons. We found that PV$^+$ interneurons targeted the perisomatic region, with little input at dendritic locations, whereas SOM$^+$ interneurons synapse throughout the dendrites, with more input in the apical domain (Figures S3A and S3B). However, CC and CT neurons again displayed similar distributions of normalized IPSC amplitude along their dendrites (Figures S3A and S3B). Together, these findings indicate that inhibitory inputs are stronger at CT neurons, and that differential subcellular targeting does not explain the stronger inputs at CT neurons.

One potential concern is that PV$^+$ interneurons can sometimes be labeled in SOM-Cre mice crossed to Cre-dependent reporter lines (Hu et al., 2013). If this also occurred with viral labeling in adult mice, it could confound attempts to examine cell-type-specific inputs at pyramidal neuron subtypes. To test for off-target viral expression, we injected the PFC of SOM-Cre × Ai14 mice with AAV1-FLEX-EGFP and found that a large percentage of tdTomato$^+$ neurons were also EGFP$^+$ neurons (Figures S3C and S3D). Antibody staining for PV indicated that some tdTomato$^+$ neurons were also PV positive, whereas very few EGFP$^+$ neurons were also PV positive (Figure S3E). Furthermore, for PV-Cre × Ai14 mice injected with AAV1-FLEX-EGFP, there was minimal overlap of antibody staining for SOM in either tdTomato$^+$ or EGFP$^+$ neurons (Figure S3E). These results indicate that off-target recombination, caused by developmental effects (Batista-Brito and Fishell, 2009; Hu et al., 2013), is unlikely to influence any of our results obtained with viral injection.

Distinct Intrinsic and Synaptic Responses at CC and CT Neurons

The postsynaptic response to callosal input ultimately depends on the intrinsic properties of pyramidal neurons, which are known to vary based on projection target (Dembrow et al., 2010; Gee et al., 2012). Current-clamp recordings from CC and CT neurons showed distinct responses to depolarizing and hyperpolarizing current injections (Figures 4A and 4B). While both cell types could be driven to fire APs, CT neurons were much less excitable and had distinct subthreshold properties, with lower input resistance (R_{in}), pronounced voltage sag (sag ratio), and faster membrane time constant (Tau) (Figures 4C and S4A). CT neurons also rested at more depolarized membrane potentials (Figure 4C; Vrest: CC = −75 ± 1 mV, CT = −66 ± 1 mV, $p < 0.001$), at which they retained distinct subthreshold properties (Figure S4B). These results indicate that these projection neurons have different intrinsic properties, with lower excitability and faster kinetics at CT neurons.

To determine the functional impact of differences in synaptic connectivity and intrinsic physiology, we next examined callosal responses recorded in current clamp. We initially compared excitatory postsynaptic potentials (EPSPs) in adjacent CC and CT neurons with intact excitation and inhibition. We found that wide-field illumination generated robust cPFC-evoked EPSPs at both cell types (Figure 4D). Despite stronger inputs onto CT neurons, EPSP amplitudes were similar at the two cell types (Figure 4E; CC = 10.7 ± 2.7 mV, CT = 9.8 ± 1.3 mV, $p = 0.9$). In contrast, EPSPs always decayed much faster at CT neurons (Figure 4E; CC = 35 ± 4 ms, CT = 16 ± 1 ms, $p = 0.008$). Importantly, these findings were not dependent on membrane potential, as equivalent results were obtained when holding CT neurons at −65 mV, where EPSPs were again similar in amplitude (9.3 ± 0.9 mV) but decayed faster (21 ± 2 ms) (Figures 4D and 4E).

Previous studies have suggested that faster cPFC-evoked EPSPs primarily reflects stronger feedforward inhibition onto CT neurons (Lee et al., 2014a). Based on this hypothesis, and our observation that inhibition builds with stimulus intensity, we expected EPSP decay would gradually accelerate at CT cells

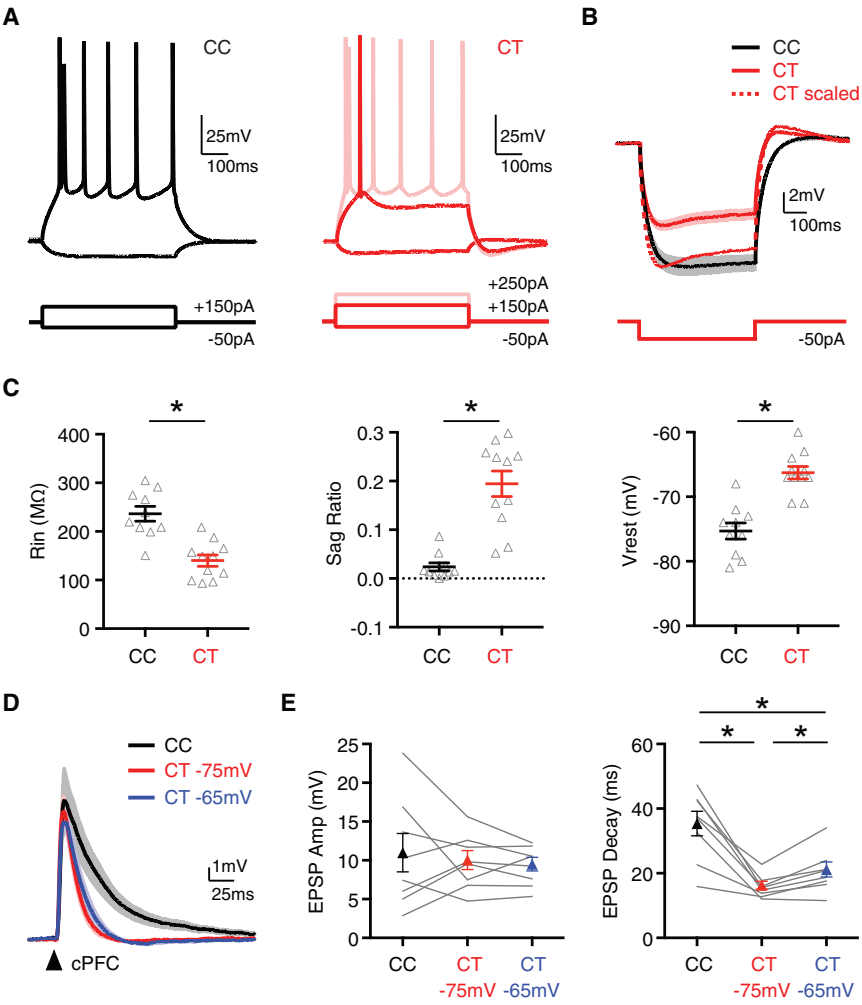

Figure 4. Callosally Evoked EPSPs Are Similar in Amplitude but Faster at CT Neurons

(A) Intrinsic physiological responses of CC (black) and CT (red) neurons held at −75 mV to depolarizing and hyperpolarizing current steps. Light red trace for CT neurons shows response to larger current injections, yielding a similar number of APs.

(B) Average response to −50 pA current step at CC and CT neurons, where solid line is average, shaded region is SEM, and dotted line is peak-scaled CT response (n = 10 CC neurons, n = 11 CT neurons) (n = 5 mice total).

(C) Summary of input resistance (R_{in}) (left) and voltage sag during hyperpolarization (sag ratio) (middle) at −75 mV and resting membrane potential (V_{rest}) (right) for neurons recorded in (B).

(D) Average cPFC-evoked EPSPs at pairs of CC neurons held at −75 mV (black) and CT neurons held at both −75 (red) and −65 mV (blue) (n = 8 pairs, 6 mice). Arrow indicates light pulse (4-ms duration).

(E) Summary of EPSP amplitudes (left) and decays (right) at pairs of CC and CT neurons, where CT neurons were recorded at both −75 (red) and −65 mV (blue).

See also Figure S4. Values are mean ± SEM, *p < 0.05.

with increasing activation of callosal inputs. However, while EPSP amplitude increased in both cell types, the decay remained constant across a broad range of light durations (Figure S4C). Consequently, there was little change in the CT/CC ratio of either EPSP amplitude or decay as a function of stimulus intensity (Figure S4D). Moreover, similar results were again obtained when holding CT neurons at more depolarized potentials (Figures S4C and S4D). Together, these findings indicate that the postsynaptic response to cPFC inputs differs markedly at neighboring CC and CT neurons. These differences persist across a range of stimulus conditions, suggesting that they may primarily reflect differences in the intrinsic properties of these neurons.

Intrinsic Properties Are Primarily Responsible for EPSP Differences

If differences in synaptic response reflect the intrinsic properties of CC and CT neurons, we expected to see similar effects on EPSPs in the absence of inhibition. We next isolated cPFC-evoked EPSPs by blocking GABAa-Rs with gabazine (GZ; 10 μM) (Figure 5A). We found that EPSP amplitudes were again similar in CC and CT neurons (Figures 5C and S5A; CT/CC amplitude ratio = 0.9, CI: 0.4–1.9, p = 0.9), and EPSP decays remained faster at CT neurons (Figures 5C and S5A; CT/CC decay ratio = 0.5, CI: 0.4–0.7, p = 0.02). These findings indicate that EPSP kinetics do not depend on feedforward inhibition, which was blocked in these experiments and thus could not contribute to synaptic responses.

Similarly, if intrinsic properties dictate synaptic response amplitude and kinetics, we expected similar regulation of inhibitory postsynaptic potentials (IPSPs) in the absence of excitation. Using conditional optogenetics, we next evoked PV^+ or SOM^+ mediated IPSPs at CC and CT neurons, while blocking AMPA receptors with NBQX (10 μM) (Figure 5B). Because IPSPs reversed near −75 mV, we recorded at −55 mV to create a driving force for GABAa-R mediated inhibition. We found that IPSP amplitudes were similar at CC and CT neurons for both inhibitory inputs (Figures 5C, S5C, and S5E; CT/CC amplitude ratio: PV^+ = 1.35, CI: 0.7–2.6, p = 0.4; SOM^+ = 0.9, CI: 0.7–1.2, p = 0.8). Moreover, decays were again much faster at CT neurons for both PV^+ and SOM^+ IPSPs (Figures 5C, S5C, and S5E; CT/CC decay ratio: PV^+ = 0.6, CI: 0.4–0.8, p = 0.03; SOM^+ = 0.5, CI: 0.4–0.8, p = 0.008). Overall, the CT/CC amplitude and decay ratios were remarkably similar for cPFC, PV^+, and SOM^+ inputs.

Intrinsic properties are sensitive to membrane potential, which in turn influences synaptic responses (González-Burgos and Barrionuevo, 2001; London and Häusser, 2005; Stuart, 1999; Williams and Stuart, 2003). To further examine the impact of intrinsic properties, we recorded EPSPs and IPSPs at potentials

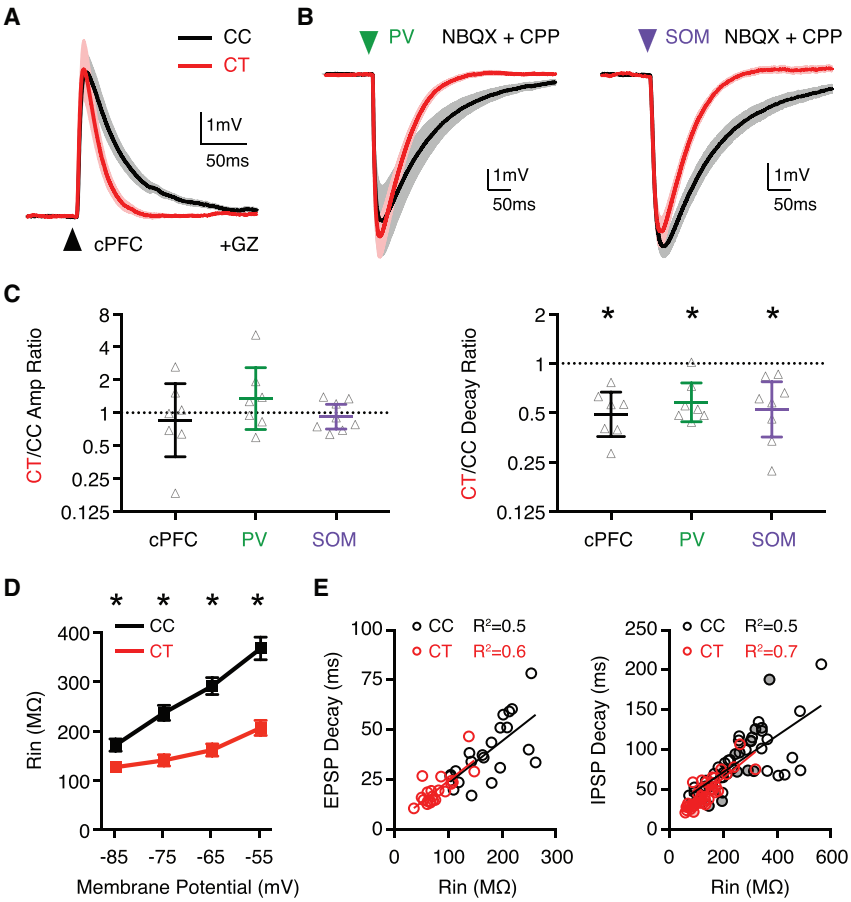

Figure 5. Isolated EPSPs and IPSPs Are Also Much Faster at CT Neurons

(A) Average cPFC-evoked EPSPs at pairs of CC (black) and CT (red) neurons held at −75 mV, with inhibition blocked by gabazine (GZ) (n = 7 pairs, 6 mice). Arrow indicates light pulse.

(B) Left, average PV^+-evoked IPSPs at pairs of CC and CT neurons held at −55 mV, with excitation blocked by NBQX and CPP (n = 7 pairs, 7 mice). Right, similar for SOM^+-evoked IPSPs held at −55 mV (n = 8 pairs, 7 mice).

(C) Summary of CT/CC amplitude (left) and decay (right) ratios for EPSPs and IPSPs, with y axis on log2 scale.

(D) Summary of the input resistance (R_{in}) of CC and CT neurons (from Figure 4C) held at multiple membrane potentials.

(E) Left, summary of EPSP decay versus input resistance from data recorded in (A), pooling data from recordings at −65, −75, and −85 mV (see also Figures S5A and S5B). Right, summary of IPSP decay versus input resistance from data recorded in (B), pooling data at −55, −65, and −85 mV (empty circles = PV^+ IPSP; closed circles = SOM^+ IPSP) (see also Figures S5C–S5F). Solid lines indicate linear fits to each dataset.

See also Figure S5. Values are geometric mean ± CI (C) or mean ± SEM (D), *p < 0.05.

ranging from −55 to −85 mV in the same cells. We found input resistance increased at depolarized potentials in both cell types but always remained lower in CT neurons (Figure 5D). The amplitudes of EPSPs and IPSPs remained similar at CC and CT neurons across a wide range of potentials (Figures S5A–S5F). The decays of EPSPs and IPSPs were slower at more depolarized potentials, but always faster at CT neurons (Figures S5A–S5F). Finally, the decays of both EPSPs and IPSPs strongly correlated with input resistance, suggesting that intrinsic properties are a major determinant of response kinetics (Figure 5E). Together, these results confirm that intrinsic properties strongly influence both EPSPs and IPSPs, with similar amplitude but faster decay in CT neurons.

H-Current Dictates Intrinsic Properties and Strongly Influences EPSPs

Hyperpolarization-activated cation (HCN) channels underlie the h-current and can strongly influence the amplitude and decay of subthreshold PSPs (Magee, 1998; Shah, 2014; Sheets et al., 2011; Srinivas et al., 2017; Williams and Stuart, 2000, 2003). We next examined the impact of h-current by performing current-clamp recordings in the presence of ZD-7288 (10 μM) to block HCN channels (Figure 6A). Under these conditions, we found that the intrinsic properties of CT neurons became largely similar to CC neurons, with a higher input resistance, negligible voltage sag, slower membrane time constant, and hyperpolarized Vrest compared to control (Figures 6B and 6C). These results indicate that blocking h-current normalizes the intrinsic properties of CC and CT neurons.

We next examined the impact of h-current on synaptic responses at adjacent CC and CT neurons. In the presence of ZD-7288, a given current step resulted in a larger and slower voltage response at CT neurons (Figure 6B), suggesting that synaptic responses should also be larger and slower under these recording conditions. Indeed, we found that the relative amplitudes of EPSPs and IPSPs were now greater at CT neurons (Figures 6D and 6E; CT/CC amplitude ratio: cPFC = 3.1, CI: 1.8–5.2, p = 0.02; PV^+ = 2.3, CI: 1.4–3.6, p = 0.02; SOM^+ = 1.5, CI: 1.2–1.9, p = 0.02). Interestingly, these responses now resembled the underlying synaptic conductances that we initially measured in voltage clamp, indicating that h-current plays a key role in equalizing synaptic responses. Moreover, the decays of these responses became more similar at CC and CT neurons (Figures 6D and 6E; CT/CC decay ratio: cPFC = 0.73, CI: 0.6–0.9, p = 0.03; PV^+ = 0.77, CI: 0.6–1.0, p = 0.1; SOM^+ = 0.85, CI: 0.7–1.1, p = 0.2). The residual differences in intrinsic properties and PSP kinetics are likely due to non-HCN mediated ionic conductances. Together, these findings indicate that the greater h-current found in CT neurons normalizes EPSP and IPSP amplitudes while accelerating their decays.

Feedforward Inhibition Has Similar Functional Impact in CC and CT Neurons

Our results show that intrinsic properties shape synaptic responses but do not establish a role for the robust feedforward

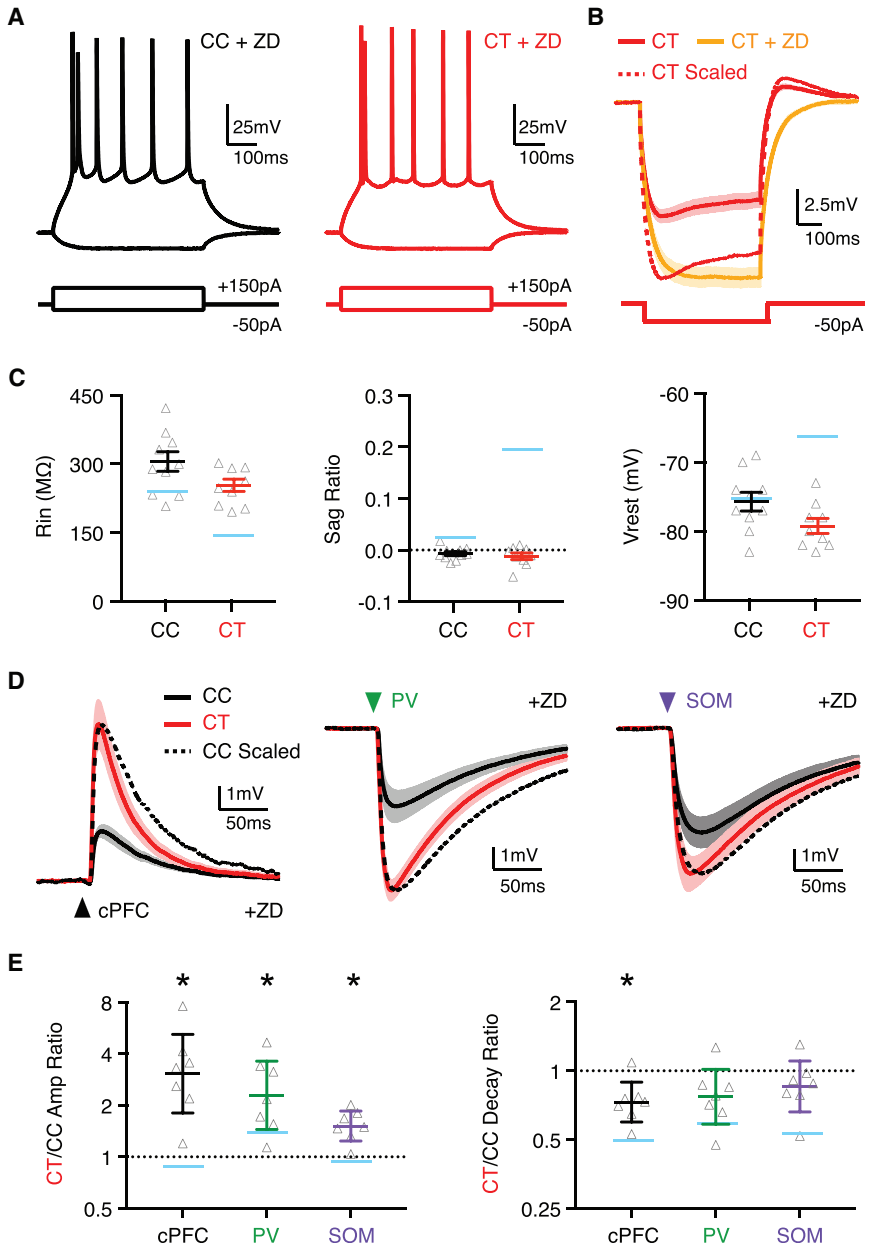

Figure 6. H-Current Influences Subthreshold Synaptic Responses at CT Neurons

(A) Intrinsic physiological responses of CC (black) and CT (red) neurons, held at −75 mV, to depolarizing and hyperpolarizing current steps, with h-current blocked by ZD-7288.

(B) Average response of CT neurons to −50 pA current step in the absence (red) and presence (orange) of ZD-7288, where dotted line is peak-scaled control (data without ZD-7288 taken from Figure 4B).

(C) Summary of input resistance (R_{in}) (left), voltage sag during hyperpolarization (sag ratio) (middle) at −75 mV, and resting membrane potential (Vrest) (right), in the presence of ZD-7288 (n = 10 CC neurons, n = 9 CT neurons) (n = 5 mice total). Light blue bars indicate values in control conditions (from Figure 4).

(D) Left, average cPFC-evoked EPSPs at pairs of CC (black) and CT (red) neurons held at −75 mV in the presence of ZD-7288, where dotted line is peak-scaled version of CC response (n = 7 pairs, 6 mice). Middle, similar for PV^+-evoked IPSPs for neurons held at −55 mV (n = 7 pairs, 7 mice). Right, similar for SOM^+-evoked IPSPs for neurons held at −55 mV (n = 7 pairs, 7 mice). Arrows indicates light pulse.

(E) Summary of CT/CC amplitude (left) and decay (right) ratios, with y axis on log2 scale. Light blue bars indicate average values in control conditions (from Figure 5).

Values are mean ± SEM (C) or geometric mean ± CI (E), *p < 0.05.

inhibition we observed. We investigated this network phenomenon by mimicking excitation and inhibition using dynamic-clamp recordings (Carter and Regehr, 2002). To validate this approach, we first injected the experimentally determined excitatory and inhibitory postsynaptic conductances (EPSG and IPSG) back into the matched postsynaptic target neuron (Figures S6A, S6B, S6E, and S6F). We found that, despite CT neurons receiving much larger synaptic conductances, EPSP and IPSP amplitudes were similar in the two cell types, whereas decays were faster at CT neurons. To highlight the importance of targeting, we switched conductances, such that CC neurons receive CT input and vice versa (Figures S6C, S6D, S6G, and S6H). The resulting EPSPs and IPSPs were larger at CC neurons, whereas decays remained faster at CT neurons, corroborating our main optogenetic findings.

To assess the impact of feedforward inhibition, we next injected either excitation alone (E) or excitation paired with inhibition (E + I) (Figure 7A). We found that inhibition reduced the EPSP amplitude similarly in CC and CT neurons (Figure 7B; (E + I) / E amplitude ratio: CC = 0.90, CI: 0.87–0.94, p = 0.002; CT = 0.87, CI: 0.84–0.90, p = 0.001), but had no effect on EPSP decay (Figure 7B; (E + I) / E decay ratio: CC = 0.98, CI: 0.93–1.02, p = 0.3; CT = 1.00, CI: 0.97–1.03, p = 0.7). To determine whether inhibition had a greater effect at more depolarized potentials, where the driving force for inhibition is increased, we also examined CT neurons at −65 mV, close to their resting membrane potential (Figure 7A). In this case, we found that inhibition reduced the EPSP amplitude more strongly ([E + I] / E amplitude ratio = 0.72, CI: 0.67–0.79, p = 0.03) and slightly accelerated EPSP decay (Figure 7B; [E + I] / E decay ratio = 0.87, CI: 0.83–0.92, p = 0.03). To evaluate the importance of targeted inhibition, we applied the same excitation but reversed the inhibitory conductances. Under these conditions, the reduction in EPSP amplitude was much smaller in CT neurons, and there

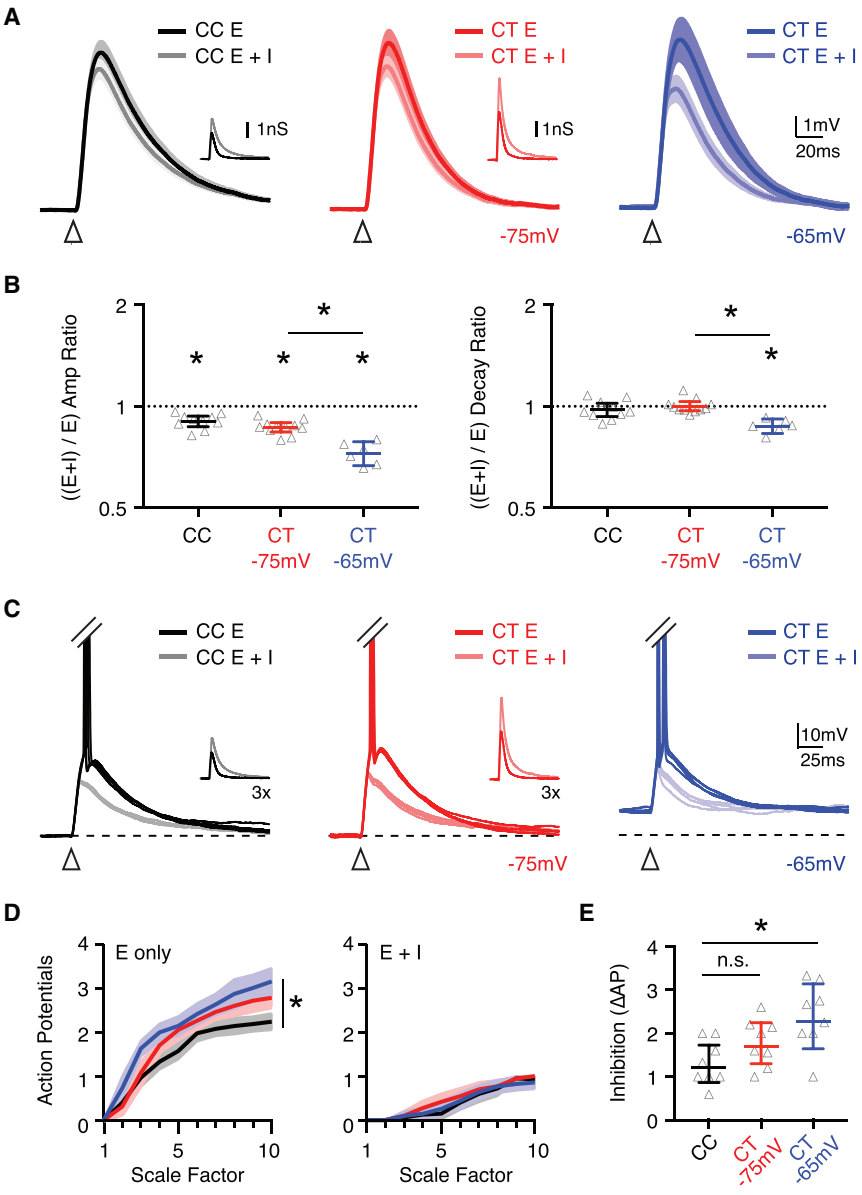

Figure 7. Targeted Inhibition Dampens EPSPs and Suppresses AP Firing

(A) Average conductance-evoked EPSPs recorded in dynamic clamp at CC neurons held at −75 mV (left) (n = 10 neurons) and CT neurons held at either −75 mV (middle) (n = 11 neurons) or −65 mV (right) (n = 6 of the 11 neurons recorded at −75 mV) (n = 6 mice total). Traces show response to either excitation alone (E) or excitation and inhibition (E + I). Inset traces show injected conductances, where dark traces are excitation and light traces are inhibition. Arrows indicate conductance onset.

(B) Summary of ([E + I] / E) amplitude (left) and decay (right) ratios, with y axis on log2 scale.

(C) Suprathreshold responses recorded in dynamic clamp, where APs have been truncated to highlight subthreshold responses. Inset traces show injected conductances with 3× scale factor.

(D) Summary of number of APs evoked at CC (n = 8 neurons) and CT (n = 8 neurons) neurons in response to different scale factors of excitation alone (left) or excitation and inhibition (right) (n = 4 mice total).

(E) Summary of inhibition of firing, calculated as the difference (Δ) in APs evoked by excitation alone (E) or excitation and inhibition (E + I) at the 10× scale factor.

See also Figures S6 and S7. Values are geometric mean ± CI (B) or mean ± SEM (D and E), *$p < 0.05$.

was less effect on EPSP decay compared to CC neurons (Figures S7A–S7D). These findings indicate that inhibition can shape subthreshold responses, with a greater impact at CT neurons. However, this effect is not caused by greater inhibition onto this population but rather depends on their more depolarized resting potential.

Finally, we examined the impact of intrinsic properties and feedforward inhibition on AP firing. Studying synaptically evoked firing is challenging in cortex, as activation of one neuronal population often triggers polysynaptic activity. We circumvented this complication using dynamic clamp to inject increasing excitation alone (E) or with inhibition (E + I), in the presence of synaptic blockers to prevent network activity (McGarry and Carter, 2016). We found that excitation alone evoked similar firing at CC and CT neurons held at −75 mV, and more robust firing at CT neurons at −65 mV (Figures 7C and 7D). The addition of inhibition potently suppressed firing at CC and CT neurons, regardless of their starting membrane potential (Figures 7C and 7D). This normalization of AP firing reflected the much stronger impact of inhibition on CT neurons held at −65 mV (Figure 7E). Last, to test the importance of biased inhibition, we reversed the inhibitory targeting and found that under these conditions the firing of CC neurons was significantly reduced compared to CT neurons (Figures S7E and S7F). Taken together, these findings highlight how cell-type-specific excitation, inhibition, and intrinsic properties of postsynaptic cells act in concert to shape the activation of different populations of projection neurons in layer 5 of the PFC.

DISCUSSION

Our findings indicate how cell-type-specific connectivity and intrinsic properties impact synaptic responses at layer 5 pyramidal neurons. Callosal inputs evoke much stronger excitation and feedforward inhibition at CT neurons compared to nearby CC neurons. Both PV^+ and SOM^+ interneurons respond to callosal inputs, and themselves make stronger connections onto CT neurons. Intrinsic properties equalize EPSP and IPSP amplitudes at the two cell types, while accelerating synaptic decays at CT neurons. Feedforward inhibition reduces EPSP amplitudes and

dampens firing, with similar effects at CC and CT neurons. Our findings reveal connectivity rules in the cortex and highlight the importance of intrinsic properties in shaping excitatory and inhibitory responses.

Callosal inputs from the contralateral hemisphere ramify across multiple layers of the PFC, including layer 5. We found both CC and CT neurons receive callosal inputs, but EPSCs are much larger at CT neurons. Previous work indicates that other intra-hemispheric connections are also biased onto non-CC neurons (Suter and Shepherd, 2015). However, other studies find that callosal inputs are larger onto CC neurons (Rock and Apicella, 2015) or show no bias (Lee et al., 2014a). In some cases, differences in targeting could reflect the variety of inputs, outputs, and functions between cortical areas (D'Souza and Burkhalter, 2017; Felleman and Van Essen, 1991). In other cases, differences could be due to the diversity within individual projection classes (Harris and Shepherd, 2015). L5 CT neurons are distinguished from CC neurons by their elaborate dendrites and pronounced h-current (Hattox and Nelson, 2007). Neurons with these properties are sometimes broadly separated into subcortically projecting type A neurons and intra-cortically projecting type B neurons. However, type A neurons also include pyramidal tract (PT) neurons that project to the pons and other subcortical regions (Dembrow et al., 2010; Harris and Shepherd, 2015; Hattox and Nelson, 2007). Furthermore, there is also evidence for diversity among intra-cortically projecting, type-B neuron populations (Kawaguchi, 2017). Therefore, by not accounting for this diversity, sorting pyramidal neurons into type A and type B classes will necessarily encompass multiple populations of neurons. We found overlap between CT and PT neurons, consistent with PT neurons sending some collaterals to thalamus (Deschênes et al., 1994; Lévesque et al., 1996). However, these two populations do not completely overlap, and CT neurons may have subtle functional differences from other classes of PT neurons (Hattox and Nelson, 2007; Rojas-Piloni et al., 2017). In the future, it will be interesting to assess synaptic responses at other classes of pyramidal neurons and determine whether connectivity primarily reflects either their outputs or intrinsic properties.

GABAergic interneurons are often thought to provide a blanket of inhibition onto local pyramidal neurons (Fino and Yuste, 2011; Packer and Yuste, 2011). However, recent results indicate that inhibition can also be stronger onto distinct classes of projection neurons (Lee et al., 2014b; McGarry and Carter, 2016; Morishima et al., 2017; Rock and Apicella, 2015; Varga et al., 2010). We found that PV^+ interneurons make stronger connections onto CT neurons, extending on previous work showing biased inputs onto physiologically defined type A neurons (Hilscher et al., 2017; Lee et al., 2014a). We also found that SOM^+ interneurons make stronger contacts onto CT neurons, suggesting that multiple inhibitory inputs selectively target this cell type. Interestingly, this biased inhibitory targeting may be genetically defined, suggesting a fundamental role in network function (Ye et al., 2015).

Stronger GABAergic connections provide an explanation for why callosally evoked inhibition is greater at CT neurons. PV^+ interneurons often mediate feedforward inhibition (Cruikshank et al., 2007; Karayannis et al., 2007; Rock and Apicella, 2015), but the contribution of other interneurons is less understood. We observed strong callosal inputs onto both PV^+ and a subset of SOM^+ interneurons, which fire and can thus participate in feedforward inhibition. The heterogeneity in the response to cPFC inputs among SOM^+ neurons may reflect the diversity of this population (Anastasiades et al., 2016; McGarry et al., 2010; Miyoshi et al., 2007; Morishima et al., 2017) and is consistent with a complex role for SOM^+ interneuron subtypes in cortical circuits (Muñoz et al., 2017; Veit et al., 2017; Xu et al., 2013). Our findings are also similar to recent studies examining BLA inputs in PFC, which can operate via PV^+ and SOM^+ interneurons (McGarry and Carter, 2016). In the future, it will be interesting to examine the impact of callosally evoked inhibition in the soma and dendrites, given that PV^+ and SOM^+ interneurons target distinct subcellular domains of pyramidal cells (Marlin and Carter, 2014; Pouille et al., 2013). It will also be important to examine how callosally evoked inhibition develops during repetitive activity, which differs for PV^+ and SOM^+ interneurons in local (Kapfer et al., 2007; Reyes et al., 1998; Silberberg and Markram, 2007) and long-range (McGarry and Carter, 2016; Porter et al., 2001) networks.

Ultimately, synaptic responses are dictated by both synaptic strength and intrinsic properties of postsynaptic neurons. We predicted that differences in intrinsic properties would selectively dampen synaptic response amplitude at CT neurons. Indeed, while EPSCs and IPSCs were larger at these cells, the resulting EPSPs and IPSPs were equivalent to CC neurons. The role of intrinsic physiology was highlighted by blocking h-current, which equalized subthreshold membrane properties and increased amplitudes at CT neurons. Furthermore, the importance of biased connectivity was established by reversing excitatory and inhibitory conductances in dynamic-clamp recordings, which unbalanced responses by increasing amplitudes at CC neurons. Together, these findings suggest that heightened connectivity may compensate for the low input resistance of CT neurons (Maffei and Fontanini, 2009; O'Leary et al., 2014; Xue et al., 2014). Intriguingly, failure of this kind of homeostasis may promote network imbalance and contribute to a number of neuropsychiatric disorders involving the PFC (Ramocki and Zoghbi, 2008).

Both feedforward inhibition and h-current can influence EPSP decay (Magee, 1998; Mittmann et al., 2005; Williams and Stuart, 2000) and consequently impact the temporal integration of synaptic inputs (Dembrow et al., 2010; Magee, 1998; Mittmann et al., 2005). However, the relative impact of connectivity and intrinsic properties on synaptic responses at different cell types has been controversial. Specifically, previous studies indicate that differences in EPSP kinetics primarily reflect either stronger feedforward inhibition at type A neurons (Lee et al., 2014a) or their elevated h-current (Dembrow et al., 2015). Several findings argue that distinct intrinsic properties are the main reason for differences in synaptic decays. First, differences in EPSP decays persisted at multiple stimulus intensities, which should vary the amount of feedforward inhibition. Second, these differences persisted for isolated EPSPs in the absence of inhibition and isolated IPSPs in the absence of excitation. Third, EPSPs and IPSPs varied with membrane potential, correlating with changes in input resistance and membrane time constant. Fourth, differences in EPSPs and IPSPs were reduced by blocking h-current,

which also restored the bias of amplitudes. Finally, similar differences in EPSPs and IPSPs were observed in dynamic-clamp recordings, in which polysynaptic circuit activity was blocked.

Although our data suggest feedforward inhibition is not responsible for differences in synaptic decays, it does impact responses in three important ways. First, inhibition reduces EPSP amplitude at both CC and CT neurons across a range of subthreshold membrane potentials. However, because the reduction is equivalent at the two cell types, it does not alter the CT/CC amplitude ratio. Second, inhibition accelerates EPSPs, but only at more depolarized membrane potentials, opposing the slowing of EPSPs that would normally occur. Third, inhibition reduces AP firing at both CC and CT neurons in response to excitatory conductance. The consequence is to normalize the functional output of the two populations across a broad range of excitation (Pouille et al., 2009). In each case, targeting of inhibition is critical, as switching the bias from CT to CC neurons fundamentally alters the balanced responses that are normally observed. Together, our findings indicate that although intrinsic properties strongly influence synaptic responses, biased inhibition also plays a critical role in the activation of these two cell types.

Several of our results highlight a key role for h-current in regulating the amplitude and kinetics of synaptic responses. HCN channels are gated by cAMP and under regulatory control by a variety of neuromodulators (Arnsten, 2011; Ulens and Siegelbaum, 2003; Wang et al., 2007). Interestingly, recent results highlight how neuromodulatory receptors can differentially impact projection neuron subtypes (Dembrow and Johnston, 2014; Dembrow et al., 2010; Kalmbach et al., 2013; Stephens et al., 2014). For example, D1 receptors are present in CC-like neurons (Seong and Carter, 2012), whereas D2 receptors are present in CT-like neurons (Gee et al., 2012). Our results suggest that by regulating h-current at CT neurons neuromodulators could strongly influence both the amplitude and kinetics of EPSPs and IPSPs. This may provide an important mechanism to dynamically rebalance cortical networks by shifting activation toward or away from CT neurons.

Together, our findings highlight the synergistic roles of connectivity and intrinsic physiology in shaping synaptic responses and evoked firing. Given the role of the PFC in executive control and neuropsychiatric disorders, several of our results are functionally important (Arnsten, 2011; Fuster, 2000; Thuault et al., 2013). Callosal inputs preferentially contact CT neurons, allowing the engagement of CT loops necessary for cognitive function (Guo et al., 2017; Parnaudeau et al., 2013; Schmitt et al., 2017). However, because CC neurons are more excitable, they are also recruited by callosal input, enabling communication between hemispheres (Li et al., 2016). Finally, although interneurons preferentially target CT neurons, they have similar functional impact on the two cell types, which helps balance the network. Thus, excitation, inhibition, and intrinsic properties work in concert to allow activation of multiple projection neurons in this circuit.

EXPERIMENTAL PROCEDURES

Animals and Surgeries

Male and female mice aged 4–6 weeks were deeply anesthetized with ketamine and xylazine, head-fixed in a stereotax (Kopf Instruments), and injected via a small craniotomy over the region of interest, as described previously (Little and Carter, 2013). Viruses, fluorescently tagged Cholera Toxin Subunit B (CTB) (Life Technologies), or fluorescent retrobeads (Lumafluor) were pressure injected using a Nanoject II (Drummond) and left for 1–3 weeks prior to recording or perfusion for anatomy. All experimental procedures were approved by the University Animal Welfare Committee of New York University.

Slice Physiology

Mice aged 6–8 weeks were anesthetized with a lethal dose of ketamine and xylazine and perfused intracardially with ice-cold sucrose solution bubbled with 95% O_2/5% CO_2. Coronal slices (300 μm) were cut and transferred to ACSF bubbled with 95% O_2/5% CO_2. Whole-cell recordings were performed at 30°C–32°C from layer 5 neurons identified by infrared-differential interference contrast and the presence of retrograde tracers or fluorescent markers. Current-clamp recordings were performed with a K-gluconate internal, while voltage-clamp recordings were performed with Cs-gluconate internal. For 2-photon imaging experiments, Alexa Fluor 594 was allowed to diffuse throughout the dendrites for at least 20 min before imaging, as previously described (Chalifoux and Carter, 2010). For optogenetic experiments, ChR2 was activated using a brief pulse of blue light via the objective. Dynamic-clamp recordings were performed using an ITC-18 (Heka Electronics) with Igor Pro (Wavemetrics) running MafPC (courtesy of Matthew Xu-Friedman).

Histology and Fluorescence Microscopy

Mice aged 6–8 weeks were anesthetized with a lethal dose of ketamine and xylazine and perfused intracardially with 0.01 M PBS followed by 4% paraformaldehyde (PFA). Brains were fixed in 4% PFA overnight (for no antibody) or for 4–5 hr (for antibody) at 4°C. Slices were prepared at 50- to 70-μm thickness (Leica VT 1000S vibratome), and either stained with anti-PV or -SOM antibodies or mounted directly under glass coverslips on gelatin-coated slides using ProLong Gold antifade reagent with DAPI (Invitrogen). Images were acquired using a slide-scanning microscope (Olympus VS120) or confocal microscope (Leica SP8).

Data Analysis

Summary data are reported as arithmetic mean ± SEM and input ratios as geometric mean with 95% confidence intervals. Statistical tests made no assumptions about the distribution of data and were performed in GraphPad Prism (version 7.0c). Unpaired comparisons were performed using two-tailed Mann-Whitney U tests. Paired comparisons were performed using two-tailed Wilcoxon matched-pairs signed-rank tests. Ratios were compared to a theoretical median of 1.0 using Wilcoxon signed-rank tests. All experiments were from at least 3 animals. Significance was defined as $p < 0.05$.

Additional methods are fully described in the Supplemental Experimental Procedures.

SUPPLEMENTAL INFORMATION

Supplemental Information includes Supplemental Experimental Procedures and seven figures and can be found with this article online at https://doi.org/10.1016/j.celrep.2017.12.073.

ACKNOWLEDGMENTS

We thank the Carter lab, Simon Peron, and Nic Tritsch for helpful discussions and comments on the manuscript. We thank Matthew Xu-Friedman for providing software and helping with dynamic-clamp recordings. This work was supported by NIH R01 MH085974 (A.G.C.).

AUTHOR CONTRIBUTIONS

P.G.A. and A.G.C. designed the experiments, P.G.A. and J.J.M. performed the experiments, P.G.A. analyzed the data, and P.G.A. and A.G.C. wrote the paper.

DECLARATION OF INTERESTS

The authors declare no competing interests.

Received: June 22, 2017
Revised: October 16, 2017
Accepted: December 20, 2017
Published: January 16, 2018

REFERENCES

Anastasiades, P.G., Marques-Smith, A., Lyngholm, D., Lickiss, T., Raffiq, S., Kätzel, D., Miesenböck, G., and Butt, S.J. (2016). GABAergic interneurons form transient layer-specific circuits in early postnatal neocortex. Nat. Commun. *7*, 10584.

Anastasiades, P.G., Marques-Smith, A., and Butt, S.J.B. (2017). Studies of cortical connectivity using optical circuit mapping methods. J. Physiol. Published online November 6, 2017. https://doi.org/10.1113/JP273463.

Arnsten, A.F. (2011). Prefrontal cortical network connections: Key site of vulnerability in stress and schizophrenia. Int. J. Dev. Neurosci. *29*, 215–223.

Batista-Brito, R., and Fishell, G. (2009). The developmental integration of cortical interneurons into a functional network. Curr. Top. Dev. Biol. *87*, 81–118.

Berger, T., Larkum, M.E., and Lüscher, H.R. (2001). High I(h) channel density in the distal apical dendrite of layer V pyramidal cells increases bidirectional attenuation of EPSPs. J. Neurophysiol. *85*, 855–868.

Brown, S.P., and Hestrin, S. (2009). Intracortical circuits of pyramidal neurons reflect their long-range axonal targets. Nature *457*, 1133–1136.

Carr, D.B., and Sesack, S.R. (1998). Callosal terminals in the rat prefrontal cortex: Synaptic targets and association with GABA-immunoreactive structures. Synapse *29*, 193–205.

Carter, A.G., and Regehr, W.G. (2002). Quantal events shape cerebellar interneuron firing. Nat. Neurosci. *5*, 1309–1318.

Chalifoux, J.R., and Carter, A.G. (2010). GABAB receptors modulate NMDA receptor calcium signals in dendritic spines. Neuron *66*, 101–113.

Cruikshank, S.J., Lewis, T.J., and Connors, B.W. (2007). Synaptic basis for intense thalamocortical activation of feedforward inhibitory cells in neocortex. Nat. Neurosci. *10*, 462–468.

Cruikshank, S.J., Urabe, H., Nurmikko, A.V., and Connors, B.W. (2010). Pathway-specific feedforward circuits between thalamus and neocortex revealed by selective optical stimulation of axons. Neuron *65*, 230–245.

Czeiger, D., and White, E.L. (1993). Synapses of extrinsic and intrinsic origin made by callosal projection neurons in mouse visual cortex. J. Comp. Neurol. *330*, 502–513.

D'Souza, R.D., and Burkhalter, A. (2017). A laminar organization for selective cortico-cortical communication. Front. Neuroanat. *11*, 71.

Delevich, K., Tucciarone, J., Huang, Z.J., and Li, B. (2015). The mediodorsal thalamus drives feedforward inhibition in the anterior cingulate cortex via parvalbumin interneurons. J. Neurosci. *35*, 5743–5753.

Dembrow, N., and Johnston, D. (2014). Subcircuit-specific neuromodulation in the prefrontal cortex. Front. Neural Circuits *8*, 54.

Dembrow, N.C., Chitwood, R.A., and Johnston, D. (2010). Projection-specific neuromodulation of medial prefrontal cortex neurons. J. Neurosci. *30*, 16922–16937.

Dembrow, N.C., Zemelman, B.V., and Johnston, D. (2015). Temporal dynamics of L5 dendrites in medial prefrontal cortex regulate integration versus coincidence detection of afferent inputs. J. Neurosci. *35*, 4501–4514.

Deschênes, M., Bourassa, J., and Pinault, D. (1994). Corticothalamic projections from layer V cells in rat are collaterals of long-range corticofugal axons. Brain Res. *664*, 215–219.

Fame, R.M., MacDonald, J.L., and Macklis, J.D. (2011). Development, specification, and diversity of callosal projection neurons. Trends Neurosci. *34*, 41–50.

Felleman, D.J., and Van Essen, D.C. (1991). Distributed hierarchical processing in the primate cerebral cortex. Cereb. Cortex *1*, 1–47.

Ferino, F., Thierry, A.M., Saffroy, M., and Glowinski, J. (1987). Interhemispheric and subcortical collaterals of medial prefrontal cortical neurons in the rat. Brain Res. *417*, 257–266.

Fino, E., and Yuste, R. (2011). Dense inhibitory connectivity in neocortex. Neuron *69*, 1188–1203.

Fuster, J.M. (2000). Prefrontal neurons in networks of executive memory. Brain Res. Bull. *52*, 331–336.

Gabbott, P.L., Warner, T.A., Jays, P.R., Salway, P., and Busby, S.J. (2005). Prefrontal cortex in the rat: Projections to subcortical autonomic, motor, and limbic centers. J. Comp. Neurol. *492*, 145–177.

Gee, S., Ellwood, I., Patel, T., Luongo, F., Deisseroth, K., and Sohal, V.S. (2012). Synaptic activity unmasks dopamine D2 receptor modulation of a specific class of layer V pyramidal neurons in prefrontal cortex. J. Neurosci. *32*, 4959–4971.

George, M.S., Abbott, L.F., and Siegelbaum, S.A. (2009). HCN hyperpolarization-activated cation channels inhibit EPSPs by interactions with M-type K(+) channels. Nat. Neurosci. *12*, 577–584.

González-Burgos, G., and Barrionuevo, G. (2001). Voltage-gated sodium channels shape subthreshold EPSPs in layer 5 pyramidal neurons from rat prefrontal cortex. J. Neurophysiol. *86*, 1671–1684.

Guo, Z.V., Inagaki, H.K., Daie, K., Druckmann, S., Gerfen, C.R., and Svoboda, K. (2017). Maintenance of persistent activity in a frontal thalamocortical loop. Nature *545*, 181–186.

Harris, K.D., and Shepherd, G.M. (2015). The neocortical circuit: Themes and variations. Nat. Neurosci. *18*, 170–181.

Hasegawa, I., Fukushima, T., Ihara, T., and Miyashita, Y. (1998). Callosal window between prefrontal cortices: Cognitive interaction to retrieve long-term memory. Science *281*, 814–818.

Hattox, A.M., and Nelson, S.B. (2007). Layer V neurons in mouse cortex projecting to different targets have distinct physiological properties. J. Neurophysiol. *98*, 3330–3340.

Hilscher, M.M., Leão, R.N., Edwards, S.J., Leão, K.E., and Kullander, K. (2017). Chrna2-Martinotti Cells Synchronize Layer 5 Type A Pyramidal Cells via Rebound Excitation. PLoS Biol. *15*, e2001392.

Hooks, B.M., Mao, T., Gutnisky, D.A., Yamawaki, N., Svoboda, K., and Shepherd, G.M. (2013). Organization of cortical and thalamic input to pyramidal neurons in mouse motor cortex. J. Neurosci. *33*, 748–760.

Hu, H., Cavendish, J.Z., and Agmon, A. (2013). Not all that glitters is gold: Off-target recombination in the somatostatin-IRES-Cre mouse line labels a subset of fast-spiking interneurons. Front. Neural Circuits *7*, 195.

Isaacson, J.S., and Scanziani, M. (2011). How inhibition shapes cortical activity. Neuron *72*, 231–243.

Kalmbach, B.E., Chitwood, R.A., Dembrow, N.C., and Johnston, D. (2013). Dendritic generation of mGluR-mediated slow afterdepolarization in layer 5 neurons of prefrontal cortex. J. Neurosci. *33*, 13518–13532.

Kapfer, C., Glickfeld, L.L., Atallah, B.V., and Scanziani, M. (2007). Supralinear increase of recurrent inhibition during sparse activity in the somatosensory cortex. Nat. Neurosci. *10*, 743–753.

Karayannis, T., Huerta-Ocampo, I., and Capogna, M. (2007). GABAergic and pyramidal neurons of deep cortical layers directly receive and differently integrate callosal input. Cereb. Cortex *17*, 1213–1226.

Kawaguchi, Y. (2017). Pyramidal Cell Subtypes and Their Synaptic Connections in Layer 5 of Rat Frontal Cortex. Cereb. Cortex *27*, 5755–5771.

Kawaguchi, Y., and Kubota, Y. (1997). GABAergic cell subtypes and their synaptic connections in rat frontal cortex. Cereb. Cortex *7*, 476–486.

Larkman, A., and Mason, A. (1990). Correlations between morphology and electrophysiology of pyramidal neurons in slices of rat visual cortex. I. Establishment of cell classes. J. Neurosci. *10*, 1407–1414.

Le Bé, J.V., Silberberg, G., Wang, Y., and Markram, H. (2007). Morphological, electrophysiological, and synaptic properties of corticocallosal pyramidal cells in the neonatal rat neocortex. Cereb. Cortex *17*, 2204–2213.

Lee, A.T., Gee, S.M., Vogt, D., Patel, T., Rubenstein, J.L., and Sohal, V.S. (2014a). Pyramidal neurons in prefrontal cortex receive subtype-specific forms of excitation and inhibition. Neuron *81*, 61–68.

Lee, S.H., Marchionni, I., Bezaire, M., Varga, C., Danielson, N., Lovett-Barron, M., Losonczy, A., and Soltesz, I. (2014b). Parvalbumin-positive basket cells differentiate among hippocampal pyramidal cells. Neuron *82*, 1129–1144.

Lévesque, M., Gagnon, S., Parent, A., and Deschênes. (1996). Axonal arborizations of corticostriatal and corticothalamic fibers arising from the second somatosensory area in the rat. Cereb. Cortex *6*, 759–770.

Li, N., Daie, K., Svoboda, K., and Druckmann, S. (2016). Robust neuronal dynamics in premotor cortex during motor planning. Nature *532*, 459–464.

Little, J.P., and Carter, A.G. (2013). Synaptic mechanisms underlying strong reciprocal connectivity between the medial prefrontal cortex and basolateral amygdala. J. Neurosci. *33*, 15333–15342.

London, M., and Häusser, M. (2005). Dendritic computation. Annu. Rev. Neurosci. *28*, 503–532.

Maffei, A., and Fontanini, A. (2009). Network homeostasis: A matter of coordination. Curr. Opin. Neurobiol. *19*, 168–173.

Magee, J.C. (1998). Dendritic hyperpolarization-activated currents modify the integrative properties of hippocampal CA1 pyramidal neurons. J. Neurosci. *18*, 7613–7624.

Magee, J.C. (2000). Dendritic integration of excitatory synaptic input. Nat. Rev. Neurosci. *1*, 181–190.

Mao, T., Kusefoglu, D., Hooks, B.M., Huber, D., Petreanu, L., and Svoboda, K. (2011). Long-range neuronal circuits underlying the interaction between sensory and motor cortex. Neuron *72*, 111–123.

Marlin, J.J., and Carter, A.G. (2014). GABA-A receptor inhibition of local calcium signaling in spines and dendrites. J. Neurosci. *34*, 15898–15911.

Mason, A., and Larkman, A. (1990). Correlations between morphology and electrophysiology of pyramidal neurons in slices of rat visual cortex. II. Electrophysiology. J. Neurosci. *10*, 1415–1428.

McGarry, L.M., and Carter, A.G. (2016). Inhibitory gating of basolateral amygdala inputs to the prefrontal cortex. J. Neurosci. *36*, 9391–9406.

McGarry, L.M., Packer, A.M., Fino, E., Nikolenko, V., Sippy, T., and Yuste, R. (2010). Quantitative classification of somatostatin-positive neocortical interneurons identifies three interneuron subtypes. Front. Neural Circuits *4*, 12.

Mittmann, W., Koch, U., and Häusser, M. (2005). Feed-forward inhibition shapes the spike output of cerebellar Purkinje cells. J. Physiol. *563*, 369–378.

Miyoshi, G., Butt, S.J., Takebayashi, H., and Fishell, G. (2007). Physiologically distinct temporal cohorts of cortical interneurons arise from telencephalic Olig2-expressing precursors. J. Neurosci. *27*, 7786–7798.

Morishima, M., and Kawaguchi, Y. (2006). Recurrent connection patterns of corticostriatal pyramidal cells in frontal cortex. J. Neurosci. *26*, 4394–4405.

Morishima, M., Kobayashi, K., Kato, S., Kobayashi, K., and Kawaguchi, Y. (2017). Segregated excitatory-inhibitory recurrent subnetworks in layer 5 of the rat frontal cortex. Cereb. Cortex *27*, 5846–5857.

Muñoz, W., Tremblay, R., Levenstein, D., and Rudy, B. (2017). Layer-specific modulation of neocortical dendritic inhibition during active wakefulness. Science *355*, 954–959.

O'Leary, T., Williams, A.H., Franci, A., and Marder, E. (2014). Cell types, network homeostasis, and pathological compensation from a biologically plausible ion channel expression model. Neuron *82*, 809–821.

Packer, A.M., and Yuste, R. (2011). Dense, unspecific connectivity of neocortical parvalbumin-positive interneurons: A canonical microcircuit for inhibition? J. Neurosci. *31*, 13260–13271.

Parnaudeau, S., O'Neill, P.K., Bolkan, S.S., Ward, R.D., Abbas, A.I., Roth, B.L., Balsam, P.D., Gordon, J.A., and Kellendonk, C. (2013). Inhibition of mediodorsal thalamus disrupts thalamofrontal connectivity and cognition. Neuron *77*, 1151–1162.

Petreanu, L., Mao, T., Sternson, S.M., and Svoboda, K. (2009). The subcellular organization of neocortical excitatory connections. Nature *457*, 1142–1145.

Porter, J.T., Johnson, C.K., and Agmon, A. (2001). Diverse types of interneurons generate thalamus-evoked feedforward inhibition in the mouse barrel cortex. J. Neurosci. *21*, 2699–2710.

Pouille, F., Marin-Burgin, A., Adesnik, H., Atallah, B.V., and Scanziani, M. (2009). Input normalization by global feedforward inhibition expands cortical dynamic range. Nat. Neurosci. *12*, 1577–1585.

Pouille, F., Watkinson, O., Scanziani, M., and Trevelyan, A.J. (2013). The contribution of synaptic location to inhibitory gain control in pyramidal cells. Physiol. Rep. *1*, e00067.

Ramocki, M.B., and Zoghbi, H.Y. (2008). Failure of neuronal homeostasis results in common neuropsychiatric phenotypes. Nature *455*, 912–918.

Reyes, A., Lujan, R., Rozov, A., Burnashev, N., Somogyi, P., and Sakmann, B. (1998). Target-cell-specific facilitation and depression in neocortical circuits. Nat. Neurosci. *1*, 279–285.

Rock, C., and Apicella, A.J. (2015). Callosal projections drive neuronal-specific responses in the mouse auditory cortex. J. Neurosci. *35*, 6703–6713.

Rojas-Piloni, G., Guest, J.M., Egger, R., Johnson, A.S., Sakmann, B., and Oberlaender, M. (2017). Relationships between structure, in vivo function and long-range axonal target of cortical pyramidal tract neurons. Nat. Commun. *8*, 870.

Schmitt, L.I., Wimmer, R.D., Nakajima, M., Happ, M., Mofakham, S., and Halassa, M.M. (2017). Thalamic amplification of cortical connectivity sustains attentional control. Nature *545*, 219–223.

Seong, H.J., and Carter, A.G. (2012). D1 receptor modulation of action potential firing in a subpopulation of layer 5 pyramidal neurons in the prefrontal cortex. J. Neurosci. *32*, 10516–10521.

Shah, M.M. (2014). Cortical HCN channels: Function, trafficking and plasticity. J. Physiol. *592*, 2711–2719.

Sheets, P.L., Suter, B.A., Kiritani, T., Chan, C.S., Surmeier, D.J., and Shepherd, G.M. (2011). Corticospinal-specific HCN expression in mouse motor cortex: I(h)-dependent synaptic integration as a candidate microcircuit mechanism involved in motor control. J. Neurophysiol. *106*, 2216–2231.

Silberberg, G., and Markram, H. (2007). Disynaptic inhibition between neocortical pyramidal cells mediated by Martinotti cells. Neuron *53*, 735–746.

Srinivas, K.V., Buss, E.W., Sun, Q., Santoro, B., Takahashi, H., Nicholson, D.A., and Siegelbaum, S.A. (2017). The dendrites of CA2 and CA1 pyramidal neurons differentially regulate information flow in the cortico-hippocampal circuit. J. Neurosci. *37*, 3276–3293.

Stephens, E.K., Avesar, D., and Gulledge, A.T. (2014). Activity-dependent serotonergic excitation of callosal projection neurons in the mouse prefrontal cortex. Front. Neural Circuits *8*, 97.

Stuart, G. (1999). Voltage-activated sodium channels amplify inhibition in neocortical pyramidal neurons. Nat. Neurosci. *2*, 144–150.

Suter, B.A., and Shepherd, G.M. (2015). Reciprocal interareal connections to corticospinal neurons in mouse M1 and S2. J. Neurosci. *35*, 2959–2974.

Thuault, S.J., Malleret, G., Constantinople, C.M., Nicholls, R., Chen, I., Zhu, J., Panteleyev, A., Vronskaya, S., Nolan, M.F., Bruno, R., et al. (2013). Prefrontal cortex HCN1 channels enable intrinsic persistent neural firing and executive memory function. J. Neurosci. *33*, 13583–13599.

Ulens, C., and Siegelbaum, S.A. (2003). Regulation of hyperpolarization-activated HCN channels by cAMP through a gating switch in binding domain symmetry. Neuron *40*, 959–970.

Varga, C., Lee, S.Y., and Soltesz, I. (2010). Target-selective GABAergic control of entorhinal cortex output. Nat. Neurosci. *13*, 822–824.

Veit, J., Hakim, R., Jadi, M.P., Sejnowski, T.J., and Adesnik, H. (2017). Cortical gamma band synchronization through somatostatin interneurons. Nat. Neurosci. *20*, 951–959.

Wang, M., Ramos, B.P., Paspalas, C.D., Shu, Y., Simen, A., Duque, A., Vijayraghavan, S., Brennan, A., Dudley, A., Nou, E., et al. (2007).

Alpha2A-adrenoceptors strengthen working memory networks by inhibiting cAMP-HCN channel signaling in prefrontal cortex. Cell *129*, 397–410.

Wickersham, I.R., Finke, S., Conzelmann, K.K., and Callaway, E.M. (2007). Retrograde neuronal tracing with a deletion-mutant rabies virus. Nat. Methods *4*, 47–49.

Williams, S.R., and Stuart, G.J. (2000). Site independence of EPSP time course is mediated by dendritic I(h) in neocortical pyramidal neurons. J. Neurophysiol. *83*, 3177–3182.

Williams, S.R., and Stuart, G.J. (2003). Voltage- and site-dependent control of the somatic impact of dendritic IPSPs. J. Neurosci. *23*, 7358–7367.

Xu, H., Jeong, H.Y., Tremblay, R., and Rudy, B. (2013). Neocortical somatostatin-expressing GABAergic interneurons disinhibit the thalamorecipient layer 4. Neuron *77*, 155–167.

Xue, M., Atallah, B.V., and Scanziani, M. (2014). Equalizing excitation-inhibition ratios across visual cortical neurons. Nature *511*, 596–600.

Yamawaki, N., and Shepherd, G.M. (2015). Synaptic circuit organization of motor corticothalamic neurons. J. Neurosci. *35*, 2293–2307.

Ye, Z., Mostajo-Radji, M.A., Brown, J.R., Rouaux, C., Tomassy, G.S., Hensch, T.K., and Arlotta, P. (2015). Instructing perisomatic inhibition by direct lineage reprogramming of neocortical projection neurons. Neuron *88*, 475–483.

Cell Reports, Volume *22*

Supplemental Information

Cell-Type Specificity of Callosally Evoked Excitation and Feedforward Inhibition in the Prefrontal Cortex

Paul G. Anastasiades, Joseph J. Marlin, and Adam G. Carter

SUPPLEMENTAL EXPERIMENTAL PROCEDURES

Animals

Experiments used wild-type, heterozygous PV-Cre (Hippenmeyer et al., 2005), heterozygous SOM-Cre (Taniguchi et al., 2011), or PV- and SOM-Cre crossed with homozygous Ai14 tdTomato Cre-reporter line (Madisen et al., 2010) mice of either sex in a C57BL/6J background (all mice purchased from Jackson laboratories). Data were collected from166 mice, with recordings from 125 pairs of neurons and an additional 140 single cells. All experimental procedures were approved by the University Animal Welfare Committee of New York University.

Stereotaxic injections

Mice aged 4-6 weeks were deeply anesthetized with a mixture of ketamine (10 mg/mL) and xylazine (0.1 mg/mL), and head-fixed in a stereotax (Kopf Instruments). A small craniotomy was made over the injection site, using coordinates relative to Bregma: prelimbic PFC = −2.1, ±0.4, +2.2 mm; mediodorsal thalamus (MD) = -3.6, -0.3, -0.5 mm (dorsoventral, mediolateral, and rostrocaudal axes). For retrograde labeling, pipettes were filled with either red or green retrobeads (Lumafluor) or Cholera Toxin Subunit B (CTB) conjugated to either Alexa 488, 555 or 647 (Life Technologies). Viruses varied between experiment and included: AAV1-hSyn-hChR2(H134R)-EYFP (UPenn, $9.32x10^{12}$ GC/mL) for long-range excitatory inputs; AAV1-EF1a-DIO-hChR2(H134R)-EYFP (UPenn, $1.93x10^{13}$ GC/mL) for local inhibitory inputs; and AAV1-CAG-FLEX-tdTomato (UPenn, $7.88x10^{12}$ GC/mL) or AAV1-CAG-FLEX-EGFP (UPenn, $9.16x10^{12}$ GC/mL) for labeling of interneurons in either PV- or SOM-Cre mice. To study cPFC inputs at retrogradely labeled neurons, virus was mixed with retrobeads or CTB in a 1:1 ratio. Borosilicate pipettes with 5–10 μm tip diameters were back-filled, and 130-550 nL was pressure injected using a Nanoject II (Drummond), with 30 s between injections. The pipette was subsequently left in place for an additional 5 min, allowing time to diffuse away from the tip, before being slowly retracted from the brain. Animals were returned to their cages for between 1-3 weeks before recording.

Slice preparation

Mice aged 6-8 weeks of either sex were anesthetized with a lethal dose of ketamine (25 mg/mL) and xylazine (0.25 mg/mL), and perfused intracardially with ice-cold external solution containing the following (in mM): 65 sucrose, 76 NaCl, 25 $NaHCO_3$, 1.4 NaH_2PO_4, 25 glucose, 2.5 KCl, 7 $MgCl_2$, 0.4 Na-ascorbate, and 2 Na-pyruvate (295–305 mOsm), and bubbled with 95% O_2/5% CO_2. Coronal slices (300 μm thick) were cut on a VS1200 vibratome (Leica) in ice-cold external solution, before being transferred to ACSF containing the following (in mM): 120 NaCl, 25 $NaHCO_3$, 1.4 NaH_2PO_4, 21 glucose, 2.5 KCl, 2 $CaCl_2$, 1 $MgCl_2$, 0.4 Na-ascorbate, and 2 Na-pyruvate (295–305 mOsm), bubbled with 95% O_2/5% CO_2. Slices were kept for 30 min at 35°C, before being allowed to recover for 30 min at room temperature. All recordings were conducted at 30−32°C.

Electrophysiology

Whole-cell recordings were obtained from layer 5 pyramidal neurons located in the prelimbic region of the PFC at a depth of 450–550 μm from the midline. Neurons were identified by infrared-differential interference contrast, as previously described (Chalifoux and Carter, 2010), and projection target was established by the presence of retrobeads or CTB, as previously described (Little and Carter, 2013). Pairs of neighboring neurons were chosen for sequential recording, ensuring they received similar inputs (typically < 50 μm between cells, range 15-130 μm). The order of patching CC and CT neurons was randomized across experiments to avoid any bias. Borosilicate pipettes (2–5 MΩ) were filled with one of two internal solutions. For current-clamp recordings (in mM): 135 K-gluconate, 7 KCl, 10 HEPES, 10 Na-phosphocreatine, 4 Mg_2-ATP, 0.4 Na-GTP and 0.5 EGTA, 290–295 mOsm, pH 7.3, with KOH. For voltage-clamp recordings (in mM): 135 Cs-gluconate, 10 HEPES, 10 Na-phosphocreatine, 4 Mg_2-ATP, 0.4 Na-GTP, 0.5 EGTA, 10 TEA-chloride, and 2 QX314, 290–295 mOsm, pH 7.3, with CsOH. For some experiments, 30 μM Alexa Fluor 594 was included for morphological reconstructions. For experiments involving 2-photon imaging, fluorescent dye diffused throughout the dendrites for at least 20 min before imaging. Three-dimensional reconstructions of dendritic morphologies were performed using NeuronStudio (Wearne et al., 2005), while two-dimensional tracing of dendrites for figures was performed using Neurolucida (MBF Bioscience).

Electrophysiology recordings were made with a Multiclamp 700B amplifier (Axon Instruments), filtered at 4 kHz for current-clamp and 2 kHz for voltage-clamp, and sampled at 10 kHz. The initial series resistance was <20 MΩ, and recordings were ended if series resistance rose above 25 MΩ. For current-clamp recordings, neurons were held at -75 mV, unless otherwise noted. For voltage-clamp recordings, EPSCs and IPSCs were recorded at -70 mV and +10 mV, respectively. In a subset of experiments, 1 μM TTX was added to block APs, and 100 μM 4-AP and 4 mM external Ca2+ to restore release. In many experiments, 10 μM CPP with 10 μM gabazine were used to isolate AMPA receptors, and 10 μM NBQX with 10 μM CPP were used to isolate GABAa receptors. For current-clamp recordings, 2 μM CGP-55845 was also included to block GABAb receptors. 10 μM ZD-7288 was used in voltage-clamp recordings and in some current-clamp recordings to block h-current. All chemicals were purchased from Sigma or Tocris Bioscience.

Dynamic-clamp recordings

Dynamic-clamp recordings were performed using an ITC-18 interface (Heka Electronics) with Igor Pro (Wavemetrics) running MafPC (courtesy of Matthew Xu-Friedman). Experimentally recorded EPSCs and IPSCs (4 ms LED pulse duration) were first converted into excitatory and inhibitory conductances by dividing by the driving force. Conductances were then injected into neurons, with the dynamic-clamp operating at 50 kHz. The reversal potentials for AMPA-R excitation and GABAa-R inhibition were set as +10 mV and -75 mV, respectively. For feed-forward inhibition, the onset delay of the inhibitory conductance was set to 4 ms, based on voltage-clamp experiments. For suprathreshold experiments, both excitatory and inhibitory conductances were multiplied by a range of scale factors (1-10X) to mimic increasing synaptic activity at a fixed excitation / inhibition ratio (McGarry and Carter, 2016).

Optogenetics

ChR2 was expressed in presynaptic neurons or axons and activated using a brief pulse (1 to 8 ms) from a blue LED (473 nm) (Thorlabs). Due to variability in ChR2 expression across slices and animals, LED pulse power and duration were adjusted to obtain reliable responses in each slice (typically ~100-500 pA for

voltage clamp experiments and ~5-10 mV for current clamp experiments). Using these stimulation parameters, LED power was ~ 0.4-10 mW at the back aperture of the objective. For experiments using multiple durations, LED power was set to evoke increasing responses across the range of pulse durations. For wide-field illumination, light was transmitted via a 10x 0.3 NA objective (Olympus) centered 350 μm from the midline. For subcellular mapping, a 60x 1.0 NA objective (Olympus) was targeted to the dendrites, with an effective diameter of < 200 μm.

Two-photon microscopy

Two-photon imaging was performed on a custom microscope, as previously described (Chalifoux and Carter, 2010). A Ti:Sapphire laser (Coherent) tuned to 810 nm was used to excite Alexa Fluor 594 to image morphology with a 60x 1.0 NA objective (Olympus).

Histology and fluorescence microscopy

Mice were anesthetized with a lethal dose of ketamine (25 mg/mL) and xylazine (0.25 mg/mL) and perfused intracardially with 0.01 M phosphate buffered saline (PBS) followed by 4% paraformaldehyde (PFA) in 0.01 M PBS. Brains were fixed in 4% PFA in 0.01 M PBS overnight (for no antibody staining) or for 4-5 hours (for antibody staining) at 4°C. Slices were prepared at 50-70 μm thickness (Leica VT 1000S vibratome). For PV and SOM antibody labelling, slices were washed once in PBS (0.01 M), once in PBS-T (0.2 % Triton-X100), and blocked in PBS-T with 1 % w/v bovine serum albumin (BSA) for one hour, all at room temperature. Primary antibody incubation (mouse anti-parvalbumin, MAB1572, Millipore, 1:2000; rat anti-somatostatin, MAB354, Millipore, 1:400) was performed at 4^{o}C overnight. Slices were then washed 4x in PBS at RT before incubating with secondary antibody (goat anti-rat conjugated to Alexa 647, A-21247, Fisher-Invitrogen, 1:200; goat anti-mouse conjugated to Alexa 647, AB150119, Abcam, 1:200) in PBS-T + BSA for 1 hour. Slices were washed a further 3x in PBS before being mounted. All slices were mounted under glass coverslips on gelatin-coated slides using ProLong Gold antifade reagent with DAPI (Invitrogen). Whole-brain images were acquired using a slide-scanning microscope (Olympus VS120) with a 10x 0.25 NA or 20x 0.75 NA objective. Excitation wavelengths were 387, 485, 560 and 650 nm for DAPI, FITC, TRITC and Cy5, respectively. PFC images were acquired using a confocal microscope (Leica

SP8) with 10x 0.4 NA or 20x 0.75 NA objective. Excitation wavelengths were 405, 488, 552 and 638 nm for DAPI, FITC, TRITC and Cy5, respectively. Image processing involved adjusting brightness and contrast using ImageJ (NIH). Cell counting was performed in a 400 x 150 µm region of interest across layer 5 of the prelimbic PFC for CC, CT and PT comparisons, and a 300 x 1000 µm region of interest for interneuron antibody staining experiments.

Rabies anatomy

For monosynaptic rabies virus tracing, AAV1-EF1a-FLEX-TVA-Cherry (UNC, $4.00x10^{12}$ GC/mL) was mixed with AAV1-CA-FLEX-RG (UNC, $4.00x10^{12}$ GC/mL) in a 1:1 ratio, and a total volume of 750 nL was injected into a single hemisphere of the PFC of PV-Cre or SOM-Cre mice. After allowing 2 weeks for expression of these helper viruses, 500 nL of SADΔG-GFP(EnvA) rabies virus (Salk, $4.25x10^{8}$ GC/mL) was injected at the same location. After an additional 8-10 days to allow for monosynaptic retrograde labeling, mice were perfused and slices prepared for fluorescent microscopy.

Data analysis

Electrophysiology and imaging data were acquired using National Instruments boards and MATLAB (MathWorks). Wave averaging and off-line analysis was performed using Igor Pro (WaveMetrics). Input resistance was measured using the steady-state response to a 500 ms, -50 pA current injection. The membrane time constant (tau) was measured using exponential fits to these same hyperpolarizations. Voltage sag due to h-current was calculated by taking the minimum voltage in the first 200 ms, subtracting the average voltage over the final 100 ms, and dividing by the steady-state value. PSC and PSP amplitudes were measured as the average value across 1 ms around the peak response. PSP decays were calculated using exponential fits from the peak response back to baseline. Summary data are reported in the text and figures as arithmetic mean ± SEM. Input ratios are reported as geometric mean with 95 % confidence intervals (CI). Comparisons between unpaired data were performed using two-tailed Mann-Whitney U tests. Comparisons between data recorded in pairs were performed using two-tailed Wilcoxon matched-pairs signed rank tests. Ratio data were compared to a theoretical median of 1.0 using Wilcoxon signed rank tests. Firing curves were compared using two-way ANOVA analysis with correction for

multiple comparisons. Statistical tests were performed in GraphPad Prism (version 7.0c). All experiments contain data recorded from at least 3 animals. Significance was defined as $p < 0.05$.

SUPPLEMENTAL REFERENCES

Chalifoux, J.R., and Carter, A.G. (2010). GABAB receptors modulate NMDA receptor calcium signals in dendritic spines. Neuron 66, 101-113.

Hippenmeyer, S., Vrieseling, E., Sigrist, M., Portmann, T., Laengle, C., Ladle, D.R., and Arber, S. (2005). A developmental switch in the response of DRG neurons to ETS transcription factor signaling. PLoS Biol 3, e159.

Little, J.P., and Carter, A.G. (2013). Synaptic mechanisms underlying strong reciprocal connectivity between the medial prefrontal cortex and basolateral amygdala. J Neurosci 33, 15333-15342.

Madisen, L., Zwingman, T.A., Sunkin, S.M., Oh, S.W., Zariwala, H.A., Gu, H., Ng, L.L., Palmiter, R.D., Hawrylycz, M.J., Jones, A.R.*, et al.* (2010). A robust and high-throughput Cre reporting and characterization system for the whole mouse brain. Nat Neurosci 13, 133-140.

McGarry, L.M., and Carter, A.G. (2016). Inhibitory Gating of Basolateral Amygdala Inputs to the Prefrontal Cortex. J Neurosci 36, 9391-9406.

Taniguchi, H., He, M., Wu, P., Kim, S., Paik, R., Sugino, K., Kvitsiani, D., Fu, Y., Lu, J., Lin, Y.*, et al.* (2011). A resource of Cre driver lines for genetic targeting of GABAergic neurons in cerebral cortex. Neuron 71, 995-1013.

Wearne, S.L., Rodriguez, A., Ehlenberger, D.B., Rocher, A.B., Henderson, S.C., and Hof, P.R. (2005). New techniques for imaging, digitization and analysis of three-dimensional neural morphology on multiple scales. Neuroscience 136, 661-680.

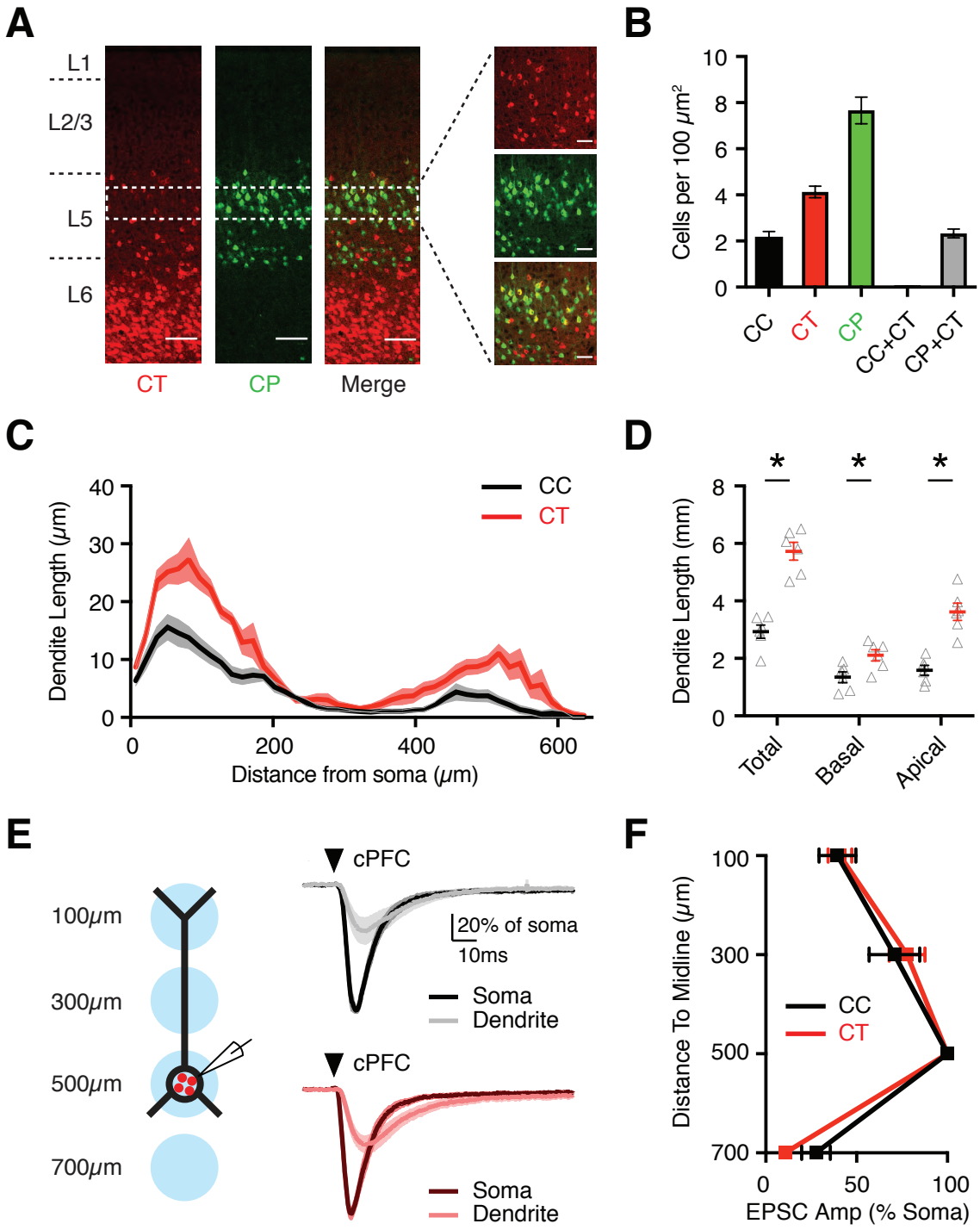

Anastasiades et al., Figure S1

SUPPLEMENTAL FIGURE LEGENDS

Figure S1: Properties of projection neurons and cPFC inputs to their dendrites

Related to Figure 1.

A) Confocal images showing the distributions of CT neurons (*left*) and CP neurons (*middle*), along with merged image (*right*) showing co-localization across layers of the prelimbic PFC (scale bar = 100 μm). Dashed white box indicates the band in layer 5 (L5) from which electrophysiological recordings were made. *Far right*, Confocal image of CT neurons (red) and CP neurons (green) and their co-localization in layer 5 (scale bar = 25 μm). (Representative images, n = 3 mice).

B) Summary of relative density of CC, CT, CP and dual-labeled neurons (CC + CT, or CP + CT) counted per slice (n = 9 slices from 3 mice for both CC / CT and CP / CT comparisons). CC and CT neurons represent distinct, non-overlapping populations of layer 5 pyramidal neurons, whereas CP and CT show partial overlap.

C) Sholl analysis of reconstructed dendrites from 2-photon images of CC (black) and CT (red) neurons (n = 6 CC neurons, n = 6 CT neurons) (n = 8 mice total).

D) Summary of total, basal and apical dendrite lengths of reconstructed dendrites of CC and CT neurons. CT neurons have more elaborate morphologies than CC neurons across multiple dendritic domains.

E) *Left*, Subcellular mapping of cPFC inputs onto different dendritic domains as specified by distances from the midline. *Right*, Average cPFC-evoked EPSCs at the soma (dark traces) and apical dendrites (light traces) of CC (*top*) (n = 7 neurons) and CT (*bottom*) (n = 7 neurons) neurons (n = 5 mice total), recorded in the presence of TTX and 4-AP. Arrows indicate light pulse.

F) Summary of cPFC-evoked EPSC amplitudes at different distances from the midline, normalized to the somatic response, from recordings in (E).

Values are mean ± SEM, * $p<0.05$.

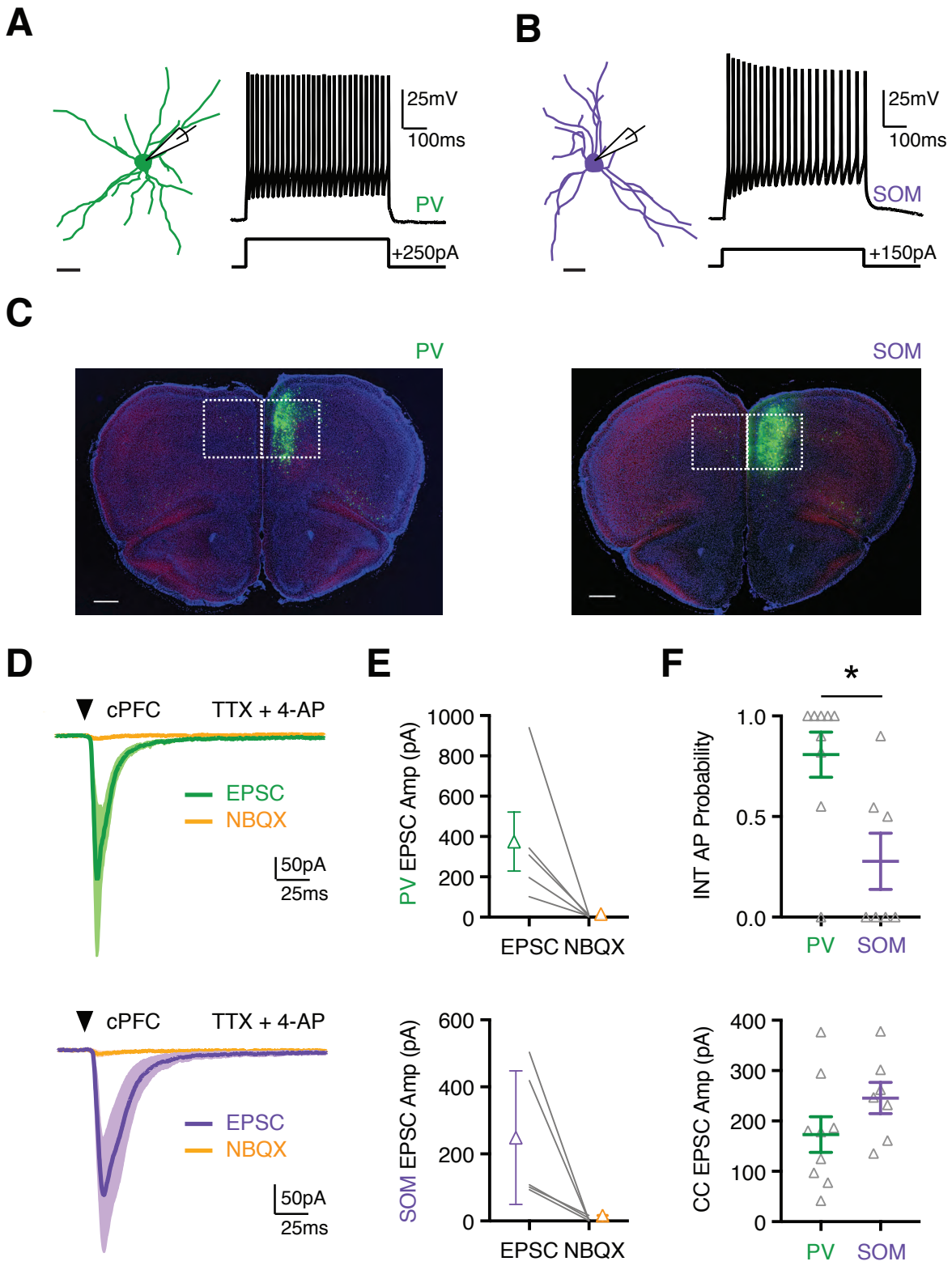

Anastasiades et al., Figure S2

Figure S2: Callosal inputs contact both PV+ and SOM+ interneurons in PFC

Related to Figure 2.

A) Dendritic reconstruction of 2-photon images (*left*) and current-clamp response (*right*) of PV+ interneuron, showing characteristic firing properties. Scale bar = 25 μm.

B) Same for SOM+ interneuron.

C) *Left*, Injection site and contralateral hemisphere of PV-Cre mouse after conditional rabies virus injection. *Right*, Similar but for a SOM-Cre mouse. Scale bars = 500 μm. Dashed boxes show regions enlarged in Fig. 2B. (Representative images, n = 3 mice).

D) *Top*, Average cPFC-evoked EPSCs at PV+ interneurons, recorded in the presence of TTX and 4-AP, and in the presence or absence of NBQX (n = 5 neurons, 4 mice). *Bottom*, Similar for SOM+ interneurons (n = 5 neurons, 3 mice). Arrow indicates light pulse (8 ms duration). Both PV+ and SOM+ interneurons receive monosynaptic glutamatergic input from the cPFC.

E) *Top*, Summary of cPFC-evoked EPSC amplitudes at PV+ interneurons, before and after bath application of NBQX. *Bottom*, Similar for SOM+ interneurons.

F) *Top,* Summary of AP probability for PV+ and SOM+ interneurons for light durations of 4 ms in the data shown in Fig. 2E & F. *Bottom,* Summary of cPFC-evoked EPSC amplitudes recorded from adjacent CC neurons for light durations of 4 ms in the data shown in Fig. 2E & F. PV+ neurons show greater firing probability, despite similar excitatory drive to the network.

Values are mean ± SEM, * $p<0.05$.

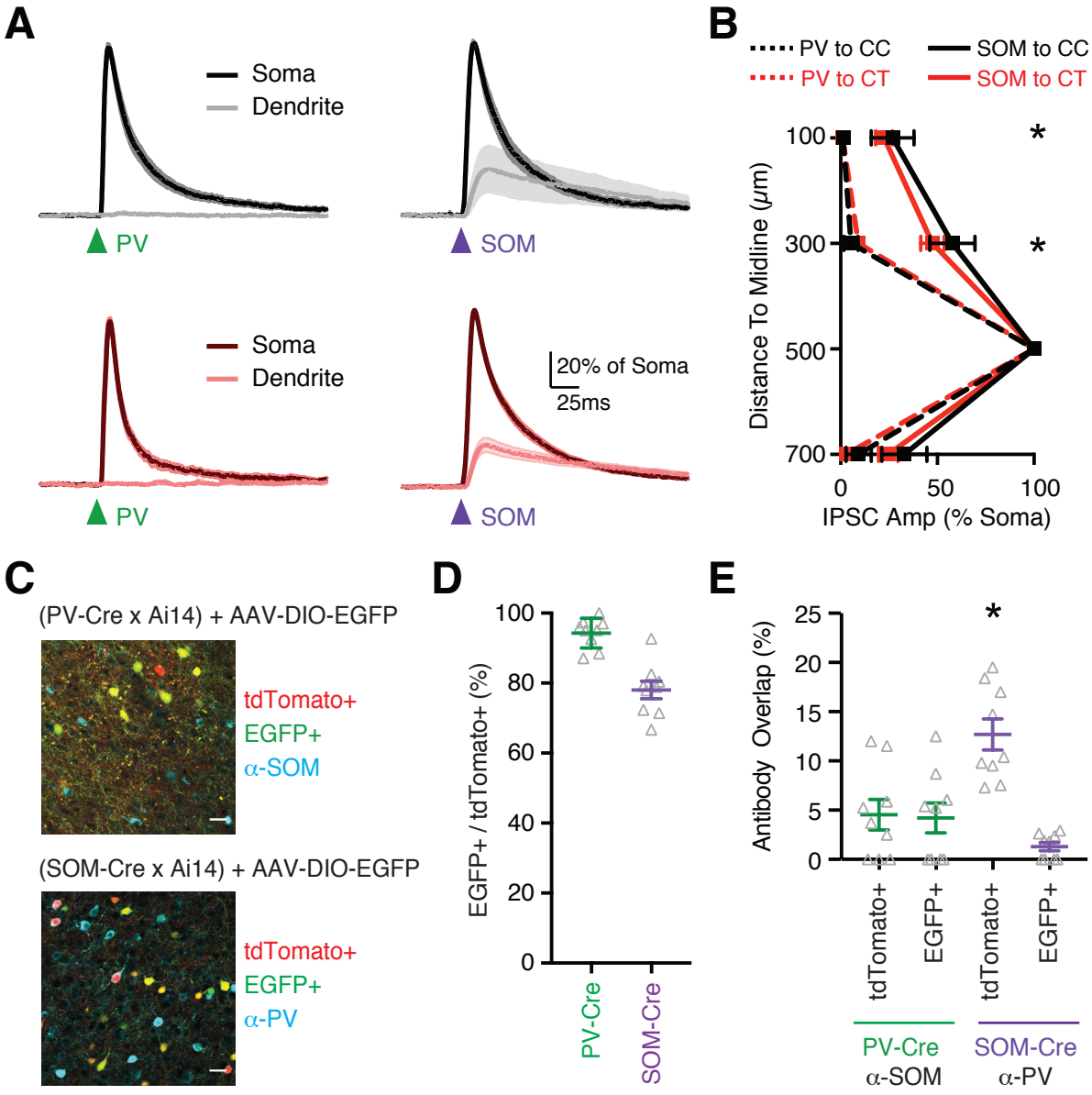

Anastasiades et al., Figure S3

Figure S3: Anatomical specificity and subcellular targeting of inhibition

Related to Figure 3.

A) *Left*, Average PV+-evoked IPSCs at the soma (dark traces) and apical dendrites (light traces) of CC neurons (*top*) (n = 7) and CT neurons (*bottom*) (n = 6) (n = 6 mice total), following schematic in Fig. S1. *Right,* Similar for SOM+-evoked IPSCs at CC neurons (n = 7) and CT neurons (n = 7) (n = 6 mice total).

B) Summary of IPSC amplitudes at different distances from the midline, normalized to the somatic response, from recordings in (A). PV+ inputs primarily target the soma, and SOM+ inputs also target the dendrites, but responses are similar in CC and CT neurons.

C) *Top*, Confocal images of layer 5 PFC, taken from PV-Cre x Ai14 mice that have been injected with AAV-FLEX-EGFP, showing tdTomato+ neurons due to Ai14 (red), EGFP+ neurons due to virus (green), and SOM+ antibody-stained neurons (cyan) (n = 9 slices from 3 mice). *Bottom*, Similar images for SOM-Cre x Ai14 mice, with PV+ antibody-stained neurons (cyan) (n = 9 slices from 3 mice). Scale bars = 25 μm.

D) Summary of percentage of tdTomato+ neurons that are also EGFP+ neurons, from experiments shown in (C). Viral infection labels a large proportion of PV+ and SOM+ interneurons that are labeled by the Ai14 reporter line. Labeling of fewer SOM+ interneurons is consistent with their known mislabeling by the Ai14 reporter line.

E) Summary of percentage of tdTomato+ or EGFP+ neurons that are co-labeled with antibodies for the opposing interneuron subtype in PV- or SOM-Cre x Ai14 mice. There is minimal labeling of PV+ interneurons by the SOM antibody using either viral or transgenic labeling. However, there is marked labeling of SOM+ interneurons by the PV antibody using the Ai14 reporter line, but not with the virus. This suggests that some PV+ interneurons will be targeted with the Ai14 reporter line, but not with our viral approaches.

Values are mean ± SEM, * $p<0.05$.

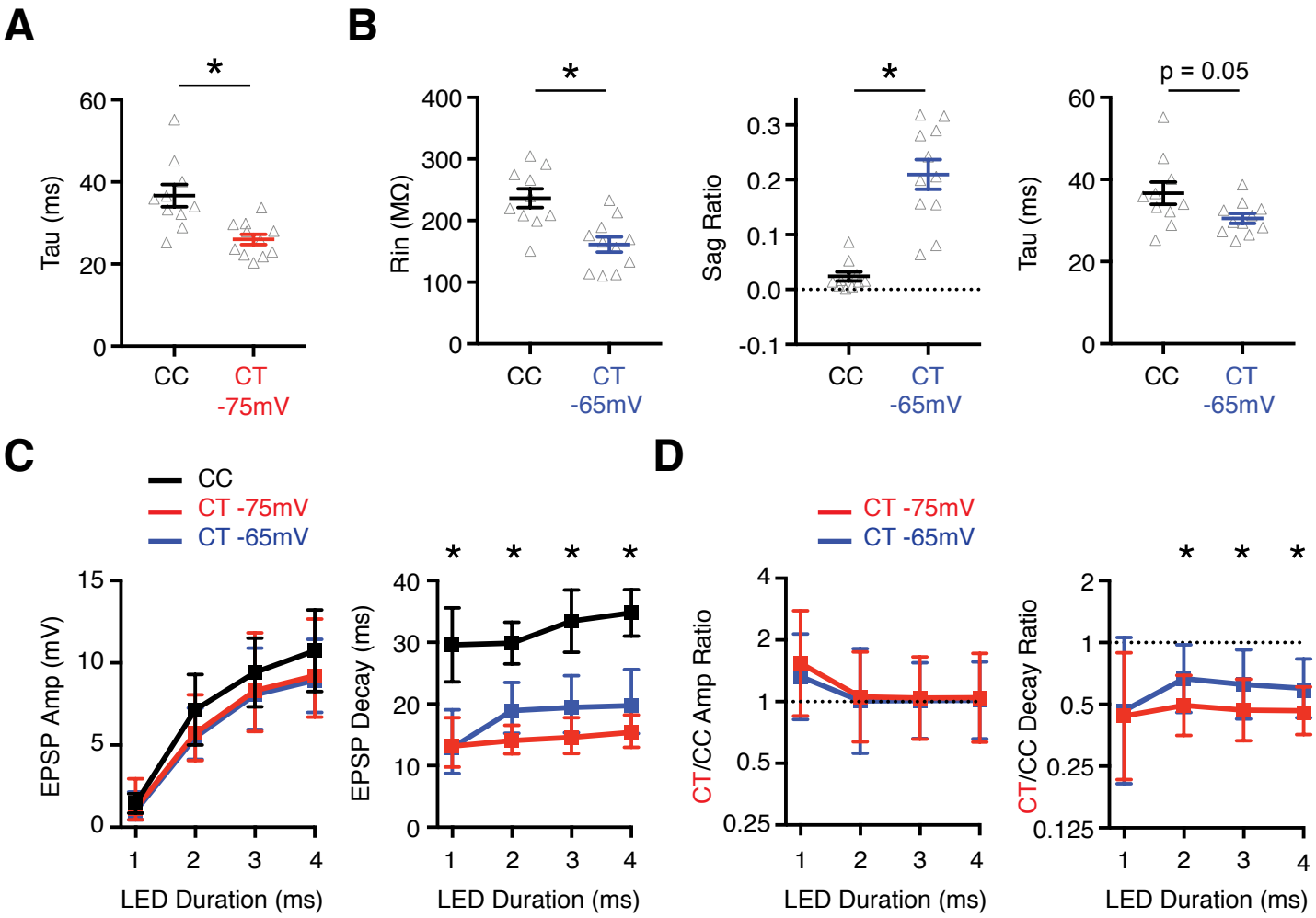

Anastasiades et al., Figure S4

Figure S4: Distinct intrinsic and synaptic responses at CC and CT neurons

Related to Figure 4.

A) Summary of membrane time constant (Tau) of CC and CT neurons recorded at -75 mV, showing faster intrinsic kinetics at CT neurons.

B) Summary of input resistance (R_{in}), voltage sag in response to hyperpolarization (Sag Ratio), and membrane time constant (Tau) for cells shown in Fig. 4C, with CC neurons held at -75 mV and CT neurons held at -65 mV, indicating qualitatively similar differences to the same CT neurons at -75 mV shown in Fig. 4C.

C) Summary of cPFC-evoked EPSP amplitudes (*left*) and decays (*right*) across a range of light durations (from data shown in Fig. 4 D - E), with CC neurons held at -75 mV and CT neurons held at both -75mV and -65mV. Faster EPSP decay is present in CT neurons at both potentials (n = 8 pairs, 6 mice).

D) Summary of CT / CC amplitude (*left*) and decay (*right*) ratios, with y-axis on log2 scale.

Values are mean ± SEM (A-C) or geometric mean ± CI (D), * $p<0.05$.

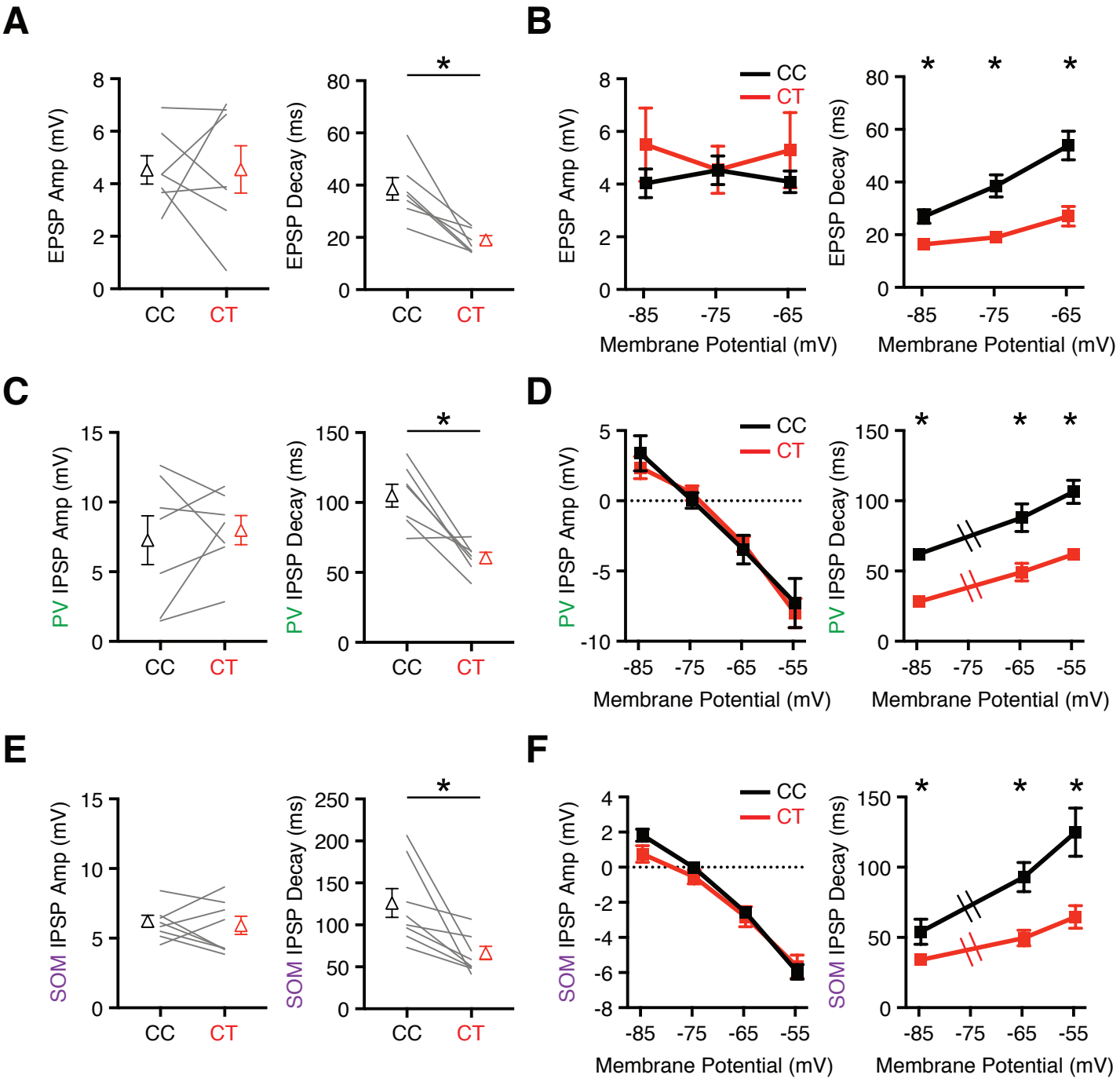

Anastasiades et al., Figure S5

Figure S5: Properties of EPSPs and IPSPs depend on membrane potential

Related to Figure 5.

A) Summary of cPFC-evoked EPSP amplitudes (*left*) and decays (*right*) for pairs of CC and CT neurons recorded at -75 mV (n = 7 pairs, as shown in Fig. 5A).

B) Summary of cPFC-evoked EPSP amplitudes (*left*) and decays (*right*) recorded across multiple membrane potentials at pairs of CC and CT neurons. EPSP amplitudes are similar at these cell types across a range of membrane potentials but decays remain distinct. Data is displayed from the same neurons recorded at each potential.

C) Similar to (A) for PV+ IPSPs recorded at -55 mV (n = 7 pairs, as shown in Fig. 5B).

D) Similar to (B) for PV+ IPSPs. IPSP amplitudes are similar at these cell types across a range of membrane potentials but decays remain distinct.

E) Similar to (A) for SOM+ IPSPs recorded at -55 mV (n = 8 pairs, as shown in Fig. 5B).

F) Similar to (D) for SOM+ IPSPs. IPSP amplitudes are similar at these cell types across a range of membrane potentials but decays remain distinct.

Note that IPSP decay is not reported at -75 mV due to its proximity to E_{Cl}.

Values are mean ± SEM, * $p<0.05$.

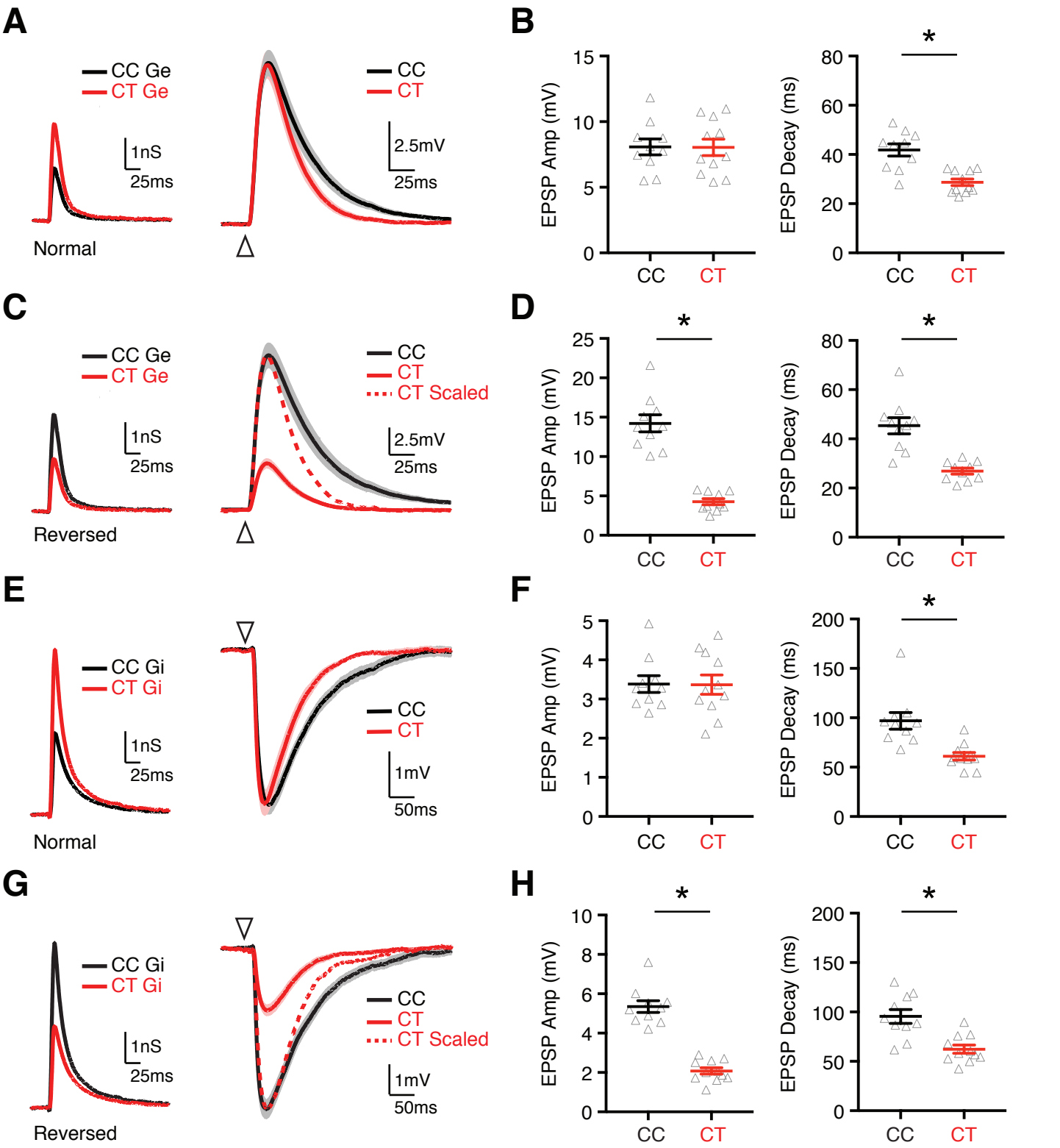

Anastasiades et al., Figure S6

Figure S6: EPSPs and IPSPs reflect both targeting and intrinsic properties

Related to Figure 7.

A) *Left*, Excitatory conductance waveforms injected into CC (black) (n = 10 neurons) and CT (red) (n = 11 neurons) (n = 6 mice total) neurons in dynamic-clamp recordings, derived from EPSCs measured in Fig. 1F. *Right*, Average conductance-evoked EPSPs recorded in dynamic-clamp at -75 mV from CC and CT neurons. Arrows indicate conductance onset.

B) Summary of EPSP amplitude (*left*) and decay (*right*) for recordings in (A). Amplitudes are similar at the two cell types, but decays are much faster at CT neurons.

C) Similar recordings to (A), where the normal conductances have now been reversed, such that CC neurons (black) receive the larger conductance, and CT neurons (red) receive the smaller. Dashed red line shows CT EPSP scaled to the peak of CC EPSP, highlighting the persistent difference in EPSP decay. Arrows indicate conductance onset.

D) Summary of EPSP amplitude (*left*) and decay (*right*) for recordings in (C). Amplitudes are now much larger at CC neurons, but decays remain much faster at CT neurons.

E – H) Similar to (A - D) for inhibitory conductances derived from IPSCs measured in Fig. 1E and conductance-evoked IPSPs recorded at -55 mV in the same CC and CT neurons as in (A). For normal targeting, amplitudes are similar at the two cell types, but decays are much faster at CT neurons. For reversed targeting, amplitudes are now much larger at CC neurons, but decays are still faster at CT neurons. Together, these data highlight the importance of both targeting of synaptic inputs and intrinsic properties of postsynaptic cells.

Values are mean ± SEM, * $p<0.05$.

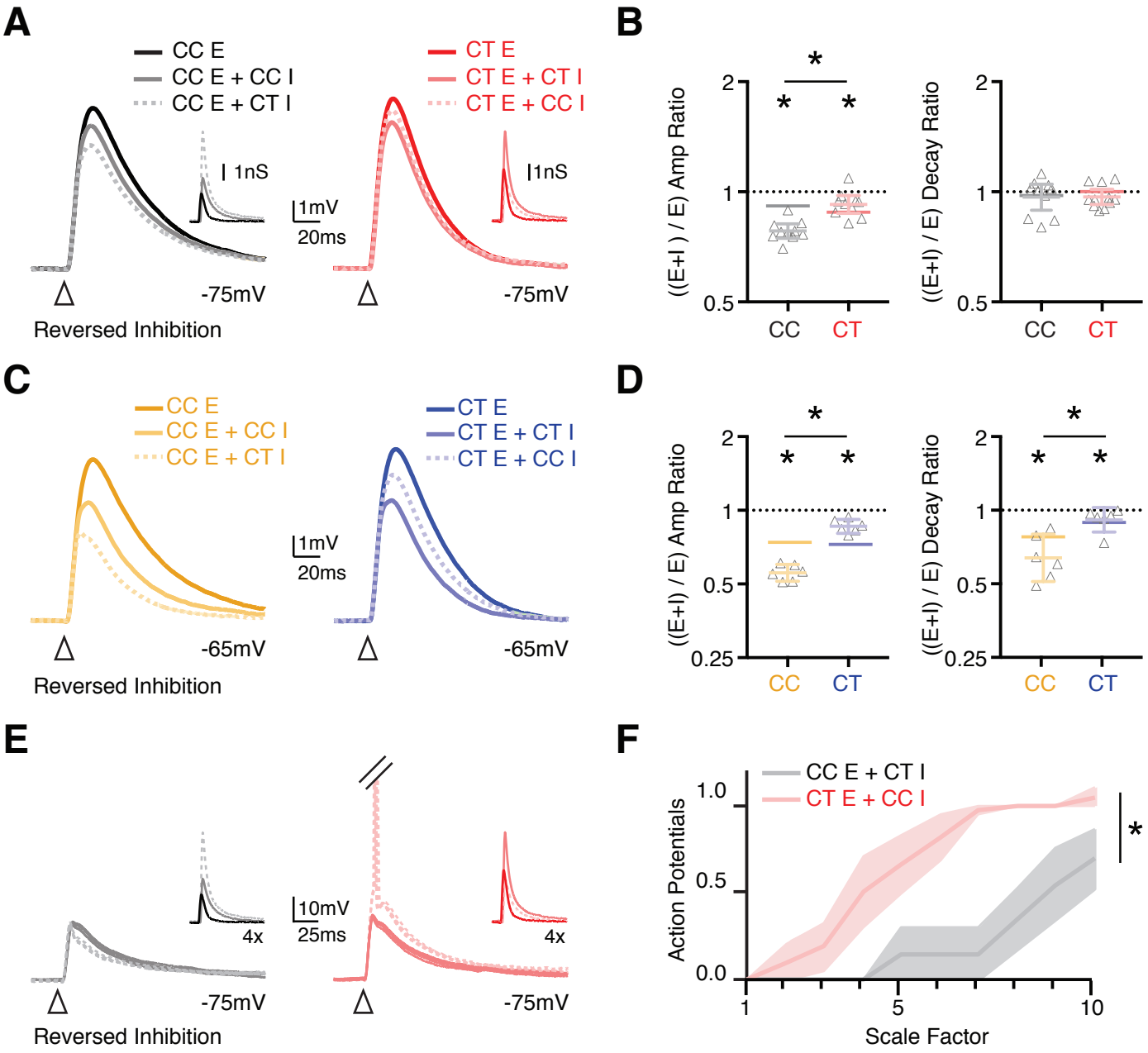

Anastasiades et al., Figure S7

Figure S7: Reversing inhibitory targeting unbalances EPSPs and evoked firing

Related to Figure 7.

A) Average conductance-evoked EPSPs recorded in dynamic-clamp at -75 mV from CC (*left*) and CT (*right*) neurons (as shown in Fig. 7A - B). EPSPs are evoked by cell-type appropriate excitation alone (black and red traces), or paired with either cell-type appropriate inhibition (grey and pink traces), or paired with reversed inhibition in which CC neurons receive CT inhibition and vice versa (dashed grey and pink traces). Arrows indicate conductance onset. Inset traces show injected conductances.

B) Summary of ((E + I) / E) amplitude (*left*) and decay (*right*) ratios for recordings in (A). Solid grey and pink bars indicate average values derived from cell-type appropriate inhibition, as shown in Fig. 7B. Reversing inhibition significantly increases the suppression of CC neurons and reduce that of CT neurons. y-axis is on log2 scale.

C – D) Similar to (A - B) for dynamic-clamp recordings at -65 mV. Reversing inhibition again leads to greater suppression of CC (n = 6) than CT (n = 6) neurons (n = 3 mice total). Moreover, reversing inhibition now preferentially accelerates the decay at CC over CT neurons.

E) Conductance-evoked EPSPs and action potentials recorded in dynamic-clamp at -75 mV from CC (*left*) (n = 8) and CT (*right*) (n = 8) neurons (as shown in Fig. 7C - E), showing response to cell-type appropriate (darker grey and pink traces) or reversed inhibition (dashed grey and pink traces). Traces are truncated to highlight subthreshold responses. Inset traces show injected conductances with 4x scale factor.

F) Summary of number of action potentials evoked at CC and CT neurons in response to different scale factors of cell-type appropriate excitation paired with reversed inhibition. Reversing inhibition increases the suppression of CC neurons, and unbalances firing at the two cell types.

Values are geometric mean ± CI (B, D) or mean ± SEM (F), * $p<0.05$.